

Effective medium approach of the resonance distribution in a random point field

David Gaspard* and Jean-Marc Sparenberg

Nuclear Physics and Quantum Physics, CP229, Université libre de Bruxelles (ULB), B-1050 Brussels, Belgium

(Dated: September 4, 2023)

In a previous paper, the distribution of resonance poles in the complex plane of the wavenumber k associated to the multiple scattering of a quantum particle in a random point field was numerically discovered. This distribution presented two distinctive structures: a set of peaks at small k when the wavelength is larger than the interscatterer distance, and a band almost parallel to the real axis at larger k . In this paper, a detailed theoretical study based on wave transport theory is proposed to explain the origin of these structures and to predict their location in the complex k plane. First, it is shown that the peaks at small k can be understood using an effective wave equation for the average wave function over the disorder. Then, that the band at large k can be described by the Bethe-Salpeter equation for the square modulus of the wavefunction, which is derived from the diagrammatic method. This study is supported by careful comparisons with numerical simulations. The largest simulations revealed the presence of quantum scars in the bulk of the disordered medium.

I. INTRODUCTION

In his seminal paper [1], Foldy derived equations governing a wave function and its square modulus in a fixed random arrangement of point scatterers on scales much larger than the wavelength. His equations shed new light on the multiple scattering of waves in random media. Under certain assumptions, his procedure was as simple as a statistical average over the positional configurations of the scatterers. Foldy's work was then reviewed by Lax [2, 3], and by other authors who studied the validity of his assumptions in more details [4–6]. Nowadays, the theory describing the propagation of a wave in a random medium is widely referred to as wave transport theory [7–11]. In the electromagnetism and optics literature, the analogous theory is known as radiative transfer theory [12–16].

In a previous paper [17], a multiple-scattering model was introduced similar to that of Foldy and Lax. This model was used in Ref. [18] to study numerically the complex resonances, which are the singular points of the full Green function at complex values of the wavenumber k . A numerical method was devised and implemented in the MSModel program [19] based on LAPACK [20] in order to map directly the full resonance distribution instead of searching for individual resonances one by one. This method allowed us to discover unknown structures in the resonance distribution as seen in Fig. 6 of Ref. [18]: an ordered set of peaks at small values of k , i.e. when the wavelength is larger than the average interscatterer distance, and a band almost parallel to the real axis at larger values of k .

In this paper, we study these structures in the resonance distribution from the theoretical point of view. In particular, we show that these structures are connected to the analogous resonances obtained in an effective medium resulting from averaging over the random

configurations of the point field. This approach leads us to derive the equations of wave transport theory in a random point field following the modern diagrammatic approach [7, 8, 10, 16, 21] extended to complex values of k . At small k , it is shown that the effective wave equation for the configurational average wave function is able to predict the position of peaks, while it must be supplanted, at large k , by the Bethe-Salpeter equation for the average density matrix.

This paper is organized as follows. In Sec. II A, the Foldy-Lax model of a quantum particle in a random point field is introduced. This model will be used throughout the text from both the theoretical and computational perspectives. The effective wave equation for the configurational average wave function is derived in two ways: the direct approach in Sec. II B 1 and the Green function approach in Sec. II B 2. In Sec. II C, we show that the effective equation predicts the low-energy peaks observed in the resonance density of Fig. 6 of Ref. [18]. In the end of Sec. II C, the positions of the peaks are related to the complex zeros of the Hankel function $H_\nu^+(z)$ presented in Appendix A. In Sec. III, the integral transport equation for the average density matrix is derived in detail, starting from the creation of a time-dependent wave packet in Sec. III A. Afterwards, the configurational average is taken in Sec. III B, leading to the Bethe-Salpeter equation. The close relationship between the Bethe-Salpeter equation and the linear Boltzmann equation is presented in Sec. III C. It is shown in Sec. III D that the mean free path can be interpreted as the coherence length of the density matrix in complete analogy with quantum mechanics [22, 23]. Then, the Bethe-Salpeter equation is approximated in the diffusive regime in Sec. III E. The approximate solutions obtained in this regime are then compared to the numerically computed wave function in Sec. III F. Finally, in Sec. III G, we show that the diffusion equation gives a prediction of the position of the band of complex resonances.

Since the models considered in this paper are valid in a space of arbitrary dimension, the volume and surface area of the unit ball in the space \mathbb{R}^d frequently appear.

* Present e-mail: david.gaspard@espci.fr

They are respectively given by

$$V_d = \frac{\pi^{\frac{d}{2}}}{\Gamma(\frac{d}{2} + 1)} \quad \text{and} \quad S_d = dV_d = \frac{2\pi^{\frac{d}{2}}}{\Gamma(\frac{d}{2})}, \quad (1)$$

where $\Gamma(z)$ denotes the gamma function [24]. The unit d -ball itself will be denoted by \mathcal{B}_d , and its external border by \mathcal{S}_d .

II. EFFECTIVE MEDIUM

A. Foldy-Lax model

Let us recall here the basics of the Foldy-Lax model [1–3, 16] that we will consider throughout this paper. This model is very convenient especially because it can be efficiently solved numerically without resorting to huge discretization lattices. In this model, a quantum particle, described by a classical wave, undergoes elastic collisions without loss of energy in a random configuration of fixed point scatterers. The wave function $\psi(\mathbf{r})$ of this particle obeys the stationary Schrödinger equation

$$[\nabla_{\mathbf{r}}^2 + k^2 - U(\mathbf{r})] \psi(\mathbf{r}) = 0, \quad (2)$$

where $k = 2\pi/\lambda$ is the wavenumber and λ the wavelength. The potential $U(\mathbf{r})$ in Eq. (2) reads

$$U(\mathbf{r}) = \sum_{i=1}^N u(\mathbf{r} - \mathbf{x}_i), \quad (3)$$

where $u(\mathbf{r})$ is a short-range potential that we will define in details soon.

In Eq. (3), the point scatterers are located at the fixed positions $\mathbf{x}_1, \mathbf{x}_2, \dots, \mathbf{x}_N$. This random point field is characterized by the joint probability distribution $P(\mathbf{x}_1, \dots, \mathbf{x}_N)$. In this regard, the statistical average of some observable A over the random configurations of the scatterers is given by

$$\langle A(\mathbf{r}) \rangle = \int_{\mathbb{R}^d} d\mathbf{x}_1 \cdots \int_{\mathbb{R}^d} d\mathbf{x}_N A(\mathbf{r}; \mathbf{x}_1, \dots, \mathbf{x}_N) P(\mathbf{x}_1, \dots, \mathbf{x}_N). \quad (4)$$

In particular, we define the local average density of scatterers per unit volume as

$$n(\mathbf{r}) = \left\langle \sum_{i=1}^N \delta(\mathbf{r} - \mathbf{x}_i) \right\rangle. \quad (5)$$

Unless otherwise stated, $\langle \cdots \rangle$ will refer to the configurational average (4). Furthermore, we assume that the positions $\mathbf{x}_1, \dots, \mathbf{x}_N$ are independent and identically distributed random variables, so that $P(\mathbf{x}_1, \dots, \mathbf{x}_N)$ factorizes into $P(\mathbf{x}_1) \cdots P(\mathbf{x}_N)$. In addition, as done in Refs. [17, 18], we assume that the scatterers are contained in a d -ball of radius R , denoted as $\mathcal{B}_d(R)$, and

that the distribution is uniform. Therefore, the scatterer density reads

$$n(\mathbf{r}) = \begin{cases} N/V & \text{if } \mathbf{r} \in \mathcal{B}_d(R), \\ 0 & \text{otherwise,} \end{cases} \quad (6)$$

where $V = V_d R^d$ is the volume of the random point field using the notation (1). In all numerical simulations, we will use the mean interparticle distance

$$\varsigma = \left(\frac{V}{N} \right)^{\frac{1}{d}}, \quad (7)$$

as the unit length.

In Eq. (3), the potential $u(\mathbf{r})$ is supposed to have a finite spatial range b much smaller than the wavelength ($kb \ll 1$), so that the point scattering theory developed in Sec. III of Ref. [17] can be applied. The short-range potential $u(\mathbf{r})$ is actually defined such that the solution of Eq. (2) for $N = 1$ reads

$$\psi(\mathbf{r}) = \phi(\mathbf{r}) + F(k)G^+(k, \mathbf{r} | \mathbf{x}_1), \quad (8)$$

where $\phi(\mathbf{r}) = e^{i\mathbf{k} \cdot \mathbf{r}}$ is the incident plane wave, $F(k)$ is the point scattering amplitude which is introduced later, and $G(k, \mathbf{r} | \mathbf{r}')$ is the free Green function satisfying

$$(\nabla_{\mathbf{r}}^2 + k^2) G(k, \mathbf{r} | \mathbf{r}') = \delta(\mathbf{r} - \mathbf{r}'). \quad (9)$$

It is worth noting that the wavenumber k in Eq. (9) is a complex number and thus reads $k = k_r + ik_i$. This will allow us to explore the time evolution of the wave packet in Sec. III. The Green function in Eq. (9) is formally given by $G(k, \mathbf{r} | \mathbf{r}') = \langle \mathbf{r} | \hat{G}(k) | \mathbf{r}' \rangle$, where $\hat{G}(k)$ is the free resolvent operator

$$\hat{G}(k) = \frac{1}{k^2 - \hat{\mathbf{p}}^2} \quad \forall k \in \mathbb{C} \setminus \mathbb{R}, \quad (10)$$

and $\hat{\mathbf{p}} = -i\nabla_{\mathbf{r}}$ is the momentum operator. Due to the isotropy and homogeneity of vacuum, $G(k, \mathbf{r} | \mathbf{r}')$ only depends on the distance $r = \|\mathbf{r} - \mathbf{r}'\|$. This is why we will use the symbol $G(k, r)$ from now on. Furthermore, the Green function $G(k, r)$ possesses two Riemann sheets upon analytic continuation to complex values of k : $G^+(k, r)$ and $G^-(k, r)$. These functions can be expressed in terms of the Hankel functions $H_{\nu}^{\pm}(z)$ [24] by

$$G^{\pm}(k, r) = \pm \frac{1}{4i} \left(\frac{k}{2\pi r} \right)^{\frac{d-2}{2}} H_{\frac{d-2}{2}}^{\pm}(kr). \quad (11)$$

In even dimensions, a branch cut separates the two functions $G^+(k, r)$ and $G^-(k, r)$. It turns out that, according to Eq. (11), this branch cut lies on the negative real semi-axis of k ($\arg k = \pi$). Therefore, this branch cut breaks the symmetries

$$\begin{cases} G^{\pm}(-k^*, r)^* = G^{\pm}(k, r), \\ G^{\pm}(-k, r) = G^{\mp}(k, r), \end{cases} \quad (12)$$

that we want to impose in this paper. In order to restore the symmetries (12) in even dimensions, we choose to move the branch cut of $G^+(k, r)$ on the negative imaginary semiaxis ($\arg k = -\frac{\pi}{2}$), and that of $G^-(k, r)$ on the positive imaginary semiaxis ($\arg k = +\frac{\pi}{2}$). This can be done with the modified Bessel function $K_\nu(z)$ [24]:

$$G^\pm(k, r) = -\frac{1}{2\pi} \left(\frac{\mp i k}{2\pi r} \right)^{\frac{d-2}{2}} K_{\frac{d-2}{2}}(\mp i k r). \quad (13)$$

The free Green function (13) is characterized by the asymptotic behavior

$$G^\pm(k, r) \xrightarrow{r \rightarrow \infty} \pm \frac{1}{2i k} \left(\frac{\mp i k}{2\pi r} \right)^{\frac{d-1}{2}} e^{\pm i k r}. \quad (14)$$

The redefinition of Eq. (11) into Eq. (13) has no consequence in odd dimensions, such as $d = 3$, but only in even dimensions. In this work, since we deal with arbitrary dimensions, including even ones, we prefer to define the Green functions as in Eq. (13), for convenience. We will see the practical consequence of this choice in the numerical simulations of Sec. II C.

In Eq. (8), $F(k)$ stands for the scattering amplitude given by Eq. (72) of Ref. [17], that is

$$F(k) = \frac{1}{\pi \mu(k)(i - \cot \delta(k))}, \quad (15)$$

where $\delta(k)$ is the s -wave phase shift and $\mu(k)$ is the free-space density of states per unit of k^2 defined by

$$\mu(k) = \langle \mathbf{r} | \delta(k^2 - \hat{\mathbf{p}}^2) | \mathbf{r} \rangle. \quad (16)$$

Due to the Sokhotski-Plemelj identity $\text{Im}[(x - i0)^{-1}] = \pi \delta(x)$, the density of states is related to the Green function by

$$\mu(k) = -\frac{1}{\pi} \lim_{r \rightarrow 0} \text{Im} G^+(k, r). \quad (17)$$

In free space, it is simply given by

$$\mu(k) = \frac{S_d k^{d-2}}{2(2\pi)^d}. \quad (18)$$

The cross section of the point scatterer is related to the scattering amplitude $F(k)$ by [17]

$$\sigma_{\text{pt}}(k) = \frac{\pi}{k} \mu(k) |F(k)|^2. \quad (19)$$

In all numerical simulations, unless otherwise mentioned, we choose to maximize the scattering amplitude (15) by imposing $\cot \delta(k) = 0$:

$$F_{\text{max}}(k) = \frac{1}{i\pi \mu(k)}. \quad (20)$$

The scattering model (20) has the particularity of saturating the upper bound for the point cross section [17]

$$\sigma_{\text{max}}(k) = \frac{1}{\pi k \mu(k)}. \quad (21)$$

Equation (20) thus produces the largest cross section possible for any given value of k . On the one hand, this is useful to effectively exploit each individual scatterer, especially in small point fields ($N \lesssim 10^2$). On the other hand, this model should be used with caution at small values of k because the cross section (21) diverges as $\mathcal{O}(k^{1-d})$ in dimensions $d \geq 2$ in a non-physical way. Another feature of the model (20) is the absence of resonance corresponding to the single-point scattering.

We have now all the ingredients to solve the full wave equation (2). Given the form of the potential (3), the particle wave function $\psi(\mathbf{r})$ should read

$$\psi(\mathbf{r}) = \phi(\mathbf{r}) + \sum_{i=1}^N a_i G^+(k, \mathbf{r} | \mathbf{x}_i), \quad (22)$$

The wave amplitudes $a_i \forall i \in \{1, \dots, N\}$ in Eq. (22) satisfy the self-consistent equation

$$a_i = F(k) \left(\phi(\mathbf{x}_i) + \sum_{j(\neq i)}^N a_j G^+(k, \mathbf{x}_i | \mathbf{x}_j) \right). \quad (23)$$

Equation (23) can be rewritten in matrix form using the vector notations $\boldsymbol{\phi} = (\phi(\mathbf{x}_1), \phi(\mathbf{x}_2), \dots, \phi(\mathbf{x}_N))^T$ and $\mathbf{a} = (a_1, a_2, \dots, a_N)^T$. The result is

$$\mathbf{M}(k) \mathbf{a} = \boldsymbol{\phi}, \quad (24)$$

where the $N \times N$ multiple-scattering matrix $\mathbf{M}(k)$ reads

$$M_{ij}(k) = F(k)^{-1} \delta_{ij} - G^+(k, \mathbf{x}_i | \mathbf{x}_j)(1 - \delta_{ij}). \quad (25)$$

All the numerical results presented in this paper are based on the solution of the linear system (24) computed with MSModel [19].

Finally, this paper primarily aims at studying the distribution of resonances which are formally defined as the singular points of the resolvent $\hat{Q}(k)$ of the complete multiple-scattering problem (2)–(3). This resolvent operator is defined by

$$\hat{Q}(k) = \frac{1}{k^2 - \hat{\mathbf{p}}^2 - U(\hat{\mathbf{r}})} \quad \forall k \in \mathbb{C} \setminus \mathbb{R}, \quad (26)$$

similarly to Eq. (10), and is related to the full Green function by $Q(k, \mathbf{r} | \mathbf{r}') = \langle \mathbf{r} | \hat{Q}(k) | \mathbf{r}' \rangle$. The latter function describes the propagation from \mathbf{r}' to \mathbf{r} in the random point field. Using the multiple-scattering matrix (25), the full resolvent (26) reads

$$\hat{Q}(k) = \hat{G}(k) + \sum_{i,j}^N \hat{G}(k) | \mathbf{x}_i \rangle [\mathbf{M}(k)^{-1}]_{ij} \langle \mathbf{x}_j | \hat{G}(k), \quad (27)$$

The inverse of the multiple-scattering matrix $\mathbf{M}(k)$ in Eq. (27) can be expanded in Dyson series as

$$\begin{aligned} \mathbf{M}^{-1} &= (F^{-1} \mathbf{1} - \mathbf{G})^{-1} \\ &= F + F^2 \mathbf{G} + F^3 \mathbf{G}^2 + F^4 \mathbf{G}^3 + \dots, \end{aligned} \quad (28)$$

where the free Green matrix $G(k)$ has the elements

$$G_{ij}(k) = G^+(k, \mathbf{x}_i | \mathbf{x}_j)(1 - \delta_{ij}). \quad (29)$$

Due to Eq. (27), the resonance poles which interest us are the solutions of the determinantal equation

$$\det M(k) = 0 \quad \text{for } k \in \mathbb{C}. \quad (30)$$

Equation (30) has infinitely many roots in the complex plane of k , and the density $\varrho^{(2)}(k_r, k_i)$ of these roots increases with the number N of scatterers. The average of this two-dimensional distribution over the random configurations of the disorder displays the structures seen, for instance, in Fig. 6 of Ref. [18].

B. Derivations of the effective wave equation

We derive the Schrödinger equation of the wave function averaged over the random configurations of the scatterers. We will call this equation the effective equation in reference to the effective medium [8]. At first sight, this approach may not seem physically relevant, because the wave function is expected to tend to zero upon averaging due to the significant destructive interferences that may occur. Nevertheless, we will see that it already provides useful information about the propagation of the wave in the medium, and brings the foundations for the more complete theory of the quantum transport that is discussed in Sec. III.

In addition, we may expect that this approach be of particular interest when the wavelength of the particle be relatively large compared to the typical interscatterer distance ($k\zeta \ll 1$). Indeed, in this regime, the wave is no longer able to resolve the spatial heterogeneities of the medium, and thus perceives a uniform *effective medium* [8]. We will show in Sec. II C that the effective medium approach successfully describes the peaks in the resonance density at low energy.

Two derivations are presented: the first one deals with the wave function, while the second one focusses on the Green function. Of course, the two derivations yield essentially the same equation.

1. Average wave function

The idea of the effective medium approach is to define the amplitude function

$$A(\mathbf{r}) = \sum_{i=1}^N a_i \delta(\mathbf{r} - \mathbf{x}_i), \quad (31)$$

which will hopefully tend to a continuous function upon configurational averaging. Let us express Eq. (23) in terms of $A(\mathbf{r})$. Multiplying both sides by $\delta(\mathbf{r} - \mathbf{x}_i)$ and

summing over i gives us

$$A(\mathbf{r}) = F(k) \left(\sum_{i=1}^N \delta(\mathbf{r} - \mathbf{x}_i) \phi(\mathbf{r}) + \sum_{i=1}^N \delta(\mathbf{r} - \mathbf{x}_i) \sum_{j(\neq i)}^N G^+(k, \mathbf{r} | \mathbf{x}_j) a_j \right). \quad (32)$$

The sum over i can be averaged over the random configurations. Since we assume that the point field is uniform with density n given by Eq. (5), Eq. (32) averages to

$$\langle A(\mathbf{r}) \rangle = n(\mathbf{r}) F(k) \left(\phi(\mathbf{r}) + \left\langle \sum_{j(\neq i)}^N G^+(k, \mathbf{r} | \mathbf{x}_j) a_j \right\rangle \right). \quad (33)$$

Note that, to get Eq. (33), we neglected the statistical correlation between a_j and \mathbf{x}_i in the last term of Eq. (32). In order to close the equation for $\langle A(\mathbf{r}) \rangle$, we need to achieve another approximation on the last term of Eq. (33). We will assume that, under the configurational average, the sum over \mathbf{x}_j can be replaced by an integral

$$\left\langle \sum_{j(\neq i)}^N G^+(k, \mathbf{r} | \mathbf{x}_j) a_j \right\rangle \simeq \int_{\mathbb{R}^d} G^+(k, \mathbf{r} | \mathbf{r}') \langle A(\mathbf{r}') \rangle d\mathbf{r}'. \quad (34)$$

The integral in the right-hand side of Eq. (34) ignores the exclusion of the i -th scatterer in the sum of the left-hand side. To some extent, this difference could be compensated by a factor $(N-1)/N$ in the right-hand side, but we deliberately omit it here because the number of scatterers is supposed to be large enough to make this factor tend to 1 [1, 2]. Finally, substituting Eq. (34) into Eq. (33) leads to

$$\langle A(\mathbf{r}) \rangle = n(\mathbf{r}) F(k) \times \left(\phi(\mathbf{r}) + \int_{\mathbb{R}^d} G^+(k, \mathbf{r} | \mathbf{r}') \langle A(\mathbf{r}') \rangle d\mathbf{r}' \right). \quad (35)$$

This is a self-consistent equation for $\langle A(\mathbf{r}) \rangle$. However, we want an equation for the average wave function itself. For this purpose, we return to Eq. (22) that we repeat here

$$\psi(\mathbf{r}) = \phi(\mathbf{r}) + \sum_{i=1}^N G^+(k, \mathbf{r} | \mathbf{x}_i) a_i. \quad (36)$$

The configurational average of Eq. (36) reads

$$\langle \psi(\mathbf{r}) \rangle = \phi(\mathbf{r}) + \int_{\mathbb{R}^d} G^+(k, \mathbf{r} | \mathbf{r}') \langle A(\mathbf{r}') \rangle d\mathbf{r}'. \quad (37)$$

Note that, in contrast to Eq. (35), the average of Eq. (36) is not subject to any approximation. This is due to the fact that Eq. (36) refers to individual scatterer positions \mathbf{x}_i , whereas Eq. (32) involves pairs of scatterers $(\mathbf{x}_i, \mathbf{x}_j)$.

When Eq. (37) is compared to Eq. (35), one notices they are directly proportional to each other. One finds

$$\langle A(\mathbf{r}) \rangle = n(\mathbf{r})F(k) \langle \psi(\mathbf{r}) \rangle. \quad (38)$$

Therefore, Eqs. (35) and (38) imply that the average wave function obeys the self-consistent equation

$$\langle \psi(\mathbf{r}) \rangle = \phi(\mathbf{r}) + \int_{\mathbb{R}^d} G^+(k, \mathbf{r} | \mathbf{r}') n(\mathbf{r}') F(k) \langle \psi(\mathbf{r}') \rangle d\mathbf{r}'. \quad (39)$$

It is worth noting that this equation closely resembles the general Lippmann-Schwinger equation but with $n(\mathbf{r})F(k)$ in the role of the potential. Therefore, this means that the average wave function $\langle \psi(\mathbf{r}) \rangle$ is effectively governed by the same Schrödinger equation (2) as the actual wave function $\psi(\mathbf{r})$, but with $U(\mathbf{r})$ replaced by $n(\mathbf{r})F(k)$. One deduces that

$$[\nabla_{\mathbf{r}}^2 + k^2 - n(\mathbf{r})F(k)] \langle \psi(\mathbf{r}) \rangle = 0. \quad (40)$$

However, the important difference between $U(\mathbf{r})$ and $n(\mathbf{r})F(k)$ is that the latter is complex while the former is real. As a consequence, Eq. (40) possesses exponentially evanescent solutions. Of course, this does not mean that the particle is absorbed in the medium, since the probability is strictly conserved in the model. In fact, this exponential evanescence of the wave is due to the destructive interferences that results from the disorder. The non-vanishing part of the average wave function $\langle \psi(\mathbf{r}) \rangle$ can be interpreted as the *coherent wave*, because it keeps in phase with the incident wave $\phi(\mathbf{r})$ [2, 5, 8, 15, 16].

2. Average Green function

Before further discussing the interpretation of Eq. (40), let us consider another, more detailed, derivation of the effective equation in terms of the Green function $Q(k, \mathbf{r} | \mathbf{r}')$ of the full multiple-scattering problem associated to the Schrödinger equation (2). Substituting Eq. (28) into Eq. (27), we get the purely abstract form

$$\hat{Q}(k) = \sum_{p=0}^{\infty} \sum_{i_1, \dots, i_p} \hat{G}(k) \hat{F}_{i_p} \hat{G}(k) \cdots \hat{G}(k) \hat{F}_{i_2} \hat{G}(k) \hat{F}_{i_1} \hat{G}(k), \quad (41)$$

where $\hat{F}_i = F(k) |\mathbf{x}_i\rangle \langle \mathbf{x}_i|$ denotes the projector onto the i -th scatterer weighted by the single-scatterer amplitude. The term $p = 0$ in Eq. (41) corresponds to the free propagation: $\hat{G}(k)$. Note that two successive indices, for instance i_1 and i_2 , cannot be equal to each other, since the Green matrix $\mathbf{G}(k)$ in Eq. (29) is zero along the diagonal. However, terms such as $i_1 = i_3$ or $i_1 = i_4$ are allowed, for instance. An elegant way of visualizing and classifying the different kinds of terms involved in Eq. (41) is to resort to diagrammatic representations. We consider for this purpose the diagrammatic notations given in Fig. 1(a) and inspired by Refs. [15, 16]. With these

(a) Notations

$$\begin{aligned} \hat{G}(k) &= \text{blue line} & \hat{F}_i(k) &= \text{blue circle with } i \\ \hat{G}^\dagger(k) &= \text{red line} & \hat{F}_i^\dagger(k) &= \text{red square with } i \end{aligned}$$

(b) Expansion of $\hat{Q}(k)$

$$\begin{aligned} \hat{Q}(k) &= \text{blue line} + \sum_{i_1} \text{blue line} \text{---} \text{blue circle } i_1 + \sum_{i_1, i_2} \text{blue line} \text{---} \text{blue circle } i_2 \text{---} \text{blue circle } i_1 \\ &+ \sum_{i_1, i_2, i_3} \text{blue line} \text{---} \text{blue circle } i_3 \text{---} \text{blue circle } i_2 \text{---} \text{blue circle } i_1 + \cdots \\ \text{One link: } &+ \sum_{i_1, i_2} \text{blue line} \text{---} \text{blue circle } i_1 \text{---} \text{blue circle } i_2 \text{---} \text{blue circle } i_1 + \sum_{i_1, i_2, i_3} \text{blue line} \text{---} \text{blue circle } i_1 \text{---} \text{blue circle } i_3 \text{---} \text{blue circle } i_2 \text{---} \text{blue circle } i_1 \\ &+ \sum_{i_1, i_2, i_3} \text{blue line} \text{---} \text{blue circle } i_2 \text{---} \text{blue circle } i_3 \text{---} \text{blue circle } i_2 \text{---} \text{blue circle } i_1 + \cdots \\ \text{Two links: } &+ \sum_{i_1, i_2} \text{blue line} \text{---} \text{blue circle } i_2 \text{---} \text{blue circle } i_1 \text{---} \text{blue circle } i_2 \text{---} \text{blue circle } i_1 \\ &+ \sum_{i_1, i_2, i_3} \text{blue line} \text{---} \text{blue circle } i_1 \text{---} \text{blue circle } i_2 \text{---} \text{blue circle } i_3 \text{---} \text{blue circle } i_2 \text{---} \text{blue circle } i_1 + \cdots \\ &+ \cdots \end{aligned}$$

FIG. 1. (a) Diagrams for the free Green function and the scattering vertex. (b) Expansion of the full resolvent $\hat{Q}(k)$ from Eq. (41). The list of diagrams is not exhaustive. The sums implicitly assume that the indices i_1, i_2, \dots are different from each other. Pairs of identical scatterers are highlighted by a black dotted link.

notations, some lowest order terms of the series (41) are shown in Fig. 1(b). In our convention, the diagrams should be read from right to left in the chronological order of the scattering events. Of course, this is not essential because of the time reversal symmetry of the Schrödinger equation. The black dotted links in Fig. 1(b) stress the fact that the scatterer encountered by the particle is the same. The existence of links between adjacent scatterers is forbidden by the zero on the diagonal of $\mathbf{G}(k)$. This is because the collision of the particle on a single scatterer is assumed to be exactly described by the scattering amplitude $F(k)$ and does not need any additional correction.

The full zoo of diagrams in Fig. 1(b) is very difficult to treat in general, especially the great herd of linked diagrams. In order to deal with the series (41), we have to neglect those linked diagrams. This approximation is known as the *Twersky approximation* [5, 15, 16]. It is based on the idea that, for a sufficiently large set of scatterers ($N \rightarrow \infty$), the chance that the particle collides two times the same scatterer is negligible. The only diagrams which are taken into account consider that the particle takes self-avoiding paths. In this regard, the sums over i_1, i_2, i_3, \dots in Fig. 1(b) implicitly assume that the indices are all different from each other.

One may verify that the number of neglected dia-

grams is relatively small for $N \rightarrow \infty$. Indeed, at a given order p , the total count of diagrams in Fig. 1(b) is $\mathcal{C}_{\text{tot}} = N(N-1)^{p-1}$, whereas the count reduces to $\mathcal{C}_{\text{sa}} = N!/(N-p)!$ if we limit ourselves to self-avoiding paths under the Twersky approximation [15, 16]. The relative difference between these counts behaves as

$$\frac{\mathcal{C}_{\text{tot}} - \mathcal{C}_{\text{sa}}}{\mathcal{C}_{\text{sa}}} = \frac{(p-1)(p-2)}{2N} + \mathcal{O}(p^4/N^2), \quad (42)$$

which obviously tends to zero for $N \rightarrow \infty$. Equation (42) confirms that the diagrams for which the particle visits the same scatterer several times are less numerous than the self-avoiding paths ($\mathcal{C}_{\text{tot}} - \mathcal{C}_{\text{sa}} \ll \mathcal{C}_{\text{sa}}$). This supports the validity of the Twersky approximation under the large N assumption [15, 16].

The Twersky approximation considerably simplifies the calculation of the average Green operator $\langle \hat{Q}(k) \rangle$. Indeed, since the positions of the scatterers are supposed to be statistically independent in our model, the configurational averages can be factored as follows

$$\begin{aligned} & \left\langle \hat{G}(k) \sum_{i_1} \hat{F}_{i_1} \hat{G}(k) \cdots \hat{G}(k) \sum_{i_p} \hat{F}_{i_p} \hat{G}(k) \right\rangle \\ &= \hat{G}(k) \left\langle \sum_{i_1} \hat{F}_{i_1} \right\rangle \hat{G}(k) \cdots \hat{G}(k) \left\langle \sum_{i_p} \hat{F}_{i_p} \right\rangle \hat{G}(k) \quad (43) \\ &= \hat{G}(k) n(\hat{\mathbf{r}}) F(k) \hat{G}(k) \cdots \hat{G}(k) n(\hat{\mathbf{r}}) F(k) \hat{G}(k), \end{aligned}$$

where one has used several times the result

$$\left\langle \sum_{i=1}^N \hat{F}_i(k) \right\rangle = \left\langle \sum_{i=1}^N F(k) \delta(\hat{\mathbf{r}} - \mathbf{x}_i) \right\rangle = n(\hat{\mathbf{r}}) F(k), \quad (44)$$

coming from Eq. (5). Note that $n(\hat{\mathbf{r}})$ does not commute with $\hat{G}(k)$ in general, because the point field has a finite size and the density thus depends on the position $\hat{\mathbf{r}}$. Substituting Eq. (43) into Eq. (41) gives us the average Green operator

$$\begin{aligned} \langle \hat{Q}(k) \rangle &= \hat{G}(k) \\ &+ \hat{G}(k) n(\hat{\mathbf{r}}) F(k) \hat{G}(k) \\ &+ \hat{G}(k) n(\hat{\mathbf{r}}) F(k) \hat{G}(k) n(\hat{\mathbf{r}}) F(k) \hat{G}(k) \\ &+ \cdots \end{aligned} \quad (45)$$

Again, this series can be more easily visualized using diagrams. We introduce to this end the additional notations given in Fig. 2(a) and inspired by Ref. [15]. With these notations, the series (45) translates to the first row of Fig. 2(b). In particular, it becomes more obvious that the series can be cast onto the recursive form

$$\langle \hat{Q}(k) \rangle = \hat{G}(k) + \hat{G}(k) n(\hat{\mathbf{r}}) F(k) \langle \hat{Q}(k) \rangle. \quad (46)$$

With a little bit of algebra, Eq. (46) can also be rewritten as

$$\langle \hat{Q}(k) \rangle = \frac{1}{\hat{G}(k)^{-1} - n(\hat{\mathbf{r}}) F(k)} = \frac{1}{k^2 - \hat{\mathbf{p}}^2 - n(\hat{\mathbf{r}}) F(k)}. \quad (47)$$

(a) Notations

$$\begin{aligned} \langle \hat{Q}(k) \rangle &= \text{---} & n(\hat{\mathbf{r}}) F(k) &= \odot \\ \langle \hat{Q}^\dagger(k) \rangle &= \text{---} & n(\hat{\mathbf{r}}) F^*(k) &= \square \end{aligned}$$

(b) Resummation of $\langle \hat{Q}(k) \rangle$

$$\begin{aligned} \langle \hat{Q}(k) \rangle &= \text{---} + \text{---} \odot + \text{---} \odot \odot + \text{---} \odot \odot \odot + \cdots \\ &= \text{---} + \text{---} \text{---} \odot. \end{aligned}$$

FIG. 2. (a) Diagrams for the effective Green function and the effective vertex. (b) Resummation of the diagrams of the average resolvent, $\langle \hat{Q}(k) \rangle$, under the Twersky approximation. This step is equivalent to Eqs. (45) and (46).

In other words, the position representation of the average Green operator in Eq. (47) reads

$$[\nabla_{\mathbf{r}}^2 + k^2 - n(\mathbf{r}) F(k)] \langle Q(k, \mathbf{r} | \mathbf{r}') \rangle = \delta(\mathbf{r} - \mathbf{r}'). \quad (48)$$

This equation is essentially the same as Eq. (40) for the average wave function $\langle \psi(\mathbf{r}) \rangle$ but with a point source at \mathbf{r}' in the right-hand side.

Furthermore, one notices the similarity between Eq. (48) and Eq. (9) for the free Green function $G(k, \mathbf{r} | \mathbf{r}')$. Accordingly, the solution of Eq. (48) has two Riemann sheets upon analytic continuation in the complex plane of k : $\langle Q^+(k, \mathbf{r} | \mathbf{r}') \rangle$ which exponentially vanishes for $\|\mathbf{r} - \mathbf{r}'\| \rightarrow \infty$, and $\langle Q^-(k, \mathbf{r} | \mathbf{r}') \rangle$ which exponentially increases.

Several additional comments should be made about the average Green function $\langle Q^+(k, \mathbf{r} | \mathbf{r}') \rangle$. First of all, if the medium is uniform and extends to infinity, then the average Green function is essentially the same as the free-space Green function

$$\langle Q^+(k, r) \rangle = G^+(\kappa(k), r), \quad (49)$$

where $r = \|\mathbf{r} - \mathbf{r}'\|$, but with k replaced by the effective wavenumber [1, 2, 5, 7, 8]

$$\kappa(k) = \sqrt{k^2 - nF(k)}. \quad (50)$$

Due to the complex nature of the scattering amplitude $F(k)$, the effective wave number κ is itself complex, meaning that the average Green function exponentially decays with the distance r from the point source. This decay is numerically confirmed with MSModel [19] in Fig. 3 for a two-dimensional (2D) point field. The adequacy is such that the theoretical average $G^+(\kappa(k), r)$ (dashed) is nearly superimposed on the numerical average of $\text{Re } Q^+(k, r)$ (solid). The exponential decay of $\langle Q^+(k, r) \rangle$ at large r is evidenced by the comparison with the free-space Green function $G^+(k, r)$ (dotted). This supports the validity of the Twersky approximation that led to Eq. (47).

Another important comment is that the characteristic length of the exponential decay of the average Green function can be physically interpreted. If we take the

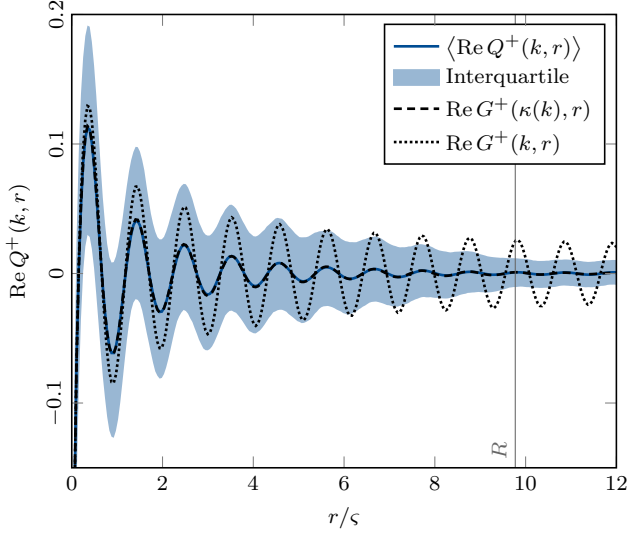


FIG. 3. Real part of the Green function in a 2D disk-shaped random point field for $N = 300$ and $k = 6\zeta^{-1}$ with a source at the center ($\mathbf{r}' = \mathbf{0}$). The solid curve is the numerical average over 2^{14} configurations, the dashed curve is the theoretical average (49), and the dotted curve is the free-space Green function (13) for comparison. The filled region is the numerically computed interquartile range of $\text{Re } Q^+(k, r)$. The radius of the medium is indicated by the gray vertical line. The model (20) is used and the mean free path is $\ell_s = 1.5\zeta$. Note that $\text{Im } k = 0$ for all curves, but $\text{Im } \kappa > 0$.

square modulus of Eq. (49) using the asymptotic behavior (14), we get

$$|\langle Q^+(k, r) \rangle|^2 \xrightarrow{r \rightarrow \infty} \frac{\pi \mu(|\kappa|)}{|\kappa| S_d r^{d-1}} e^{-2 \text{Im } \kappa r}. \quad (51)$$

The imaginary part of κ , given by Eq. (50), can be expanded if we assume that k^2 is relatively large compared to $nF(k)$. We find

$$\begin{aligned} 2 \text{Im } \kappa &= 2 \text{Im} \left(k - \frac{n}{2k} F(k) + \mathcal{O} \left[\frac{1}{k^3} (nF)^2 \right] \right) \\ &\simeq 2k_i - \frac{n}{k} \text{Im } F(k). \end{aligned} \quad (52)$$

Due to the optical theorem, given for instance by Eq. (44) of Ref. [17], it turns out that the last term of Eq. (52) is just the inverse of the scattering *mean free path* [7, 8, 11]

$$\frac{1}{\ell_s} = n\sigma = -\frac{n}{k} \text{Im } F(k). \quad (53)$$

The characteristic length ℓ_s represents the mean distance between two successive collisions of the wave in the medium. This length plays a crucial role in transport theory. Moreover, since we consider complex wavenumbers in this work, we have $k_i \neq 0$ in general. In anticipation of future calculations, we already introduce the notation

$$\gamma = 2k_i. \quad (54)$$

In this way, the behavior (51) of the average Green function reads

$$|\langle Q^+(k, r) \rangle|^2 \xrightarrow{r \rightarrow \infty} \frac{\pi \mu(|\kappa|)}{|\kappa| S_d r^{d-1}} e^{-(\gamma + n\sigma)r}. \quad (55)$$

The exponential decay of the form e^{-r/ℓ_s} in Eq. (55) is strongly reminiscent of the *Beer-Lambert law* for the attenuation (or extinction) of light in materials [16, 25]. Note, however, that the present decay actually corresponds to the loss of *phase coherence* of the wave [7, 8, 11, 15], because, due to the elastic collisions with the scatterers, the wave loses memory of its phase and thus of its direction of motion. As mentioned earlier, this decay does not indicate the presence of absorption of the wave by the medium.

It is worth noting that the mean free path $\ell_s = (n\sigma)^{-1}$ is longer than the mean interscatterer distance $\zeta = n^{-1/d}$. This results from the assumption that the point field is dilute, namely the size of the scatterers should be smaller than the interscatterer distance ($\alpha \ll \zeta$). An important consequence of $\ell_s \gg \zeta$ is that the wave is likely to pass through many scatterers before a collision effectively occurs. This is not trivial because one could *a priori* think of the propagation of the wave as being simultaneously affected by *all* the scatterers. This supposition would lead to a characteristic distance of ζ between successive interactions, or in other words $\ell_s = \zeta$, which turns out to be incorrect, as pointed out in Ref. [7, p. 86].

On the contrary, the appearance of an exponential decay (55) strongly recalls the exponential probability density

$$p_{\text{col}}(x) dx = \frac{1}{\ell_s} e^{-x/\ell_s} dx, \quad (56)$$

that the next collision takes place at the distance x from the previous collision point. Therefore, each time the wave encounters a scatterer, it gets a certain probability

$$P_{\text{col}} = 1 - e^{-\zeta/\ell_s} \simeq \frac{\zeta}{\ell_s} \quad \text{for } \zeta \ll \ell_s, \quad (57)$$

to collide with it. The probability (57) never reaches one, except of course for the nonsensical value $\ell_s = 0$. This supports the idea that, even in quantum mechanics, the collisions constitute a *Poisson process*.

C. Low-energy peaks in the resonance density

An important application of the effective equation (48) in our model is to provide an explanation of the low-energy peaks in the resonance density uncovered in Fig. 6 of Ref. [18]. In particular, we show in this section that these peaks match the complex resonances of the effective medium. For this purpose, let us solve Eq. (40) in a ball-shaped medium assuming an incident plane wave and using the partial wave method developed in Sec. 1.2 of Ref. [26]. Given the spherical symmetry of the medium,

the average wave function can be expanded in partial waves as

$$\langle \psi(\mathbf{r}) \rangle = \sum_{\ell=0}^{\infty} \langle \psi_{\ell}(r) \rangle P_{\ell}^{(d)}(\cos \theta), \quad (58)$$

where $P_{\ell}^{(d)}(\cos \theta)$ denotes the Gegenbauer polynomials generalizing the Legendre polynomials to arbitrary dimension d and defined by

$$P_{\ell}^{(d)}(x) = \frac{\Gamma(\ell + d - 2)}{\ell! \Gamma(d - 1)} {}_2F_1\left(-\ell, \ell + d - 2; \frac{1 - x}{2}; \frac{d - 1}{2}\right), \quad (59)$$

where ${}_2F_1(a, b; z)$ is the Gauss hypergeometric function [24]. In Eq. (58), $\cos \theta = \boldsymbol{\Omega} \cdot \boldsymbol{\Omega}_0$ is the cosine of the angle of $\boldsymbol{\Omega} = \mathbf{r}/r$ with respect to the direction $\boldsymbol{\Omega}_0$ of the incident plane wave. The radial components of the average wave function in Eq. (58) satisfy the radial Schrödinger equation

$$\left[\frac{d^2}{dr^2} + \frac{d - 1}{r} \frac{d}{dr} + k^2 - \frac{\ell(\ell + d - 2)}{r^2} - n(r)F(k) \right] \langle \psi_{\ell}(r) \rangle = 0, \quad (60)$$

where the density is given by Eq. (6) for a ball-shaped medium of radius R . According to this expression of the density, we have to split the wave function $\langle \psi_{\ell}(r) \rangle$ in two regions $r \leq R$ and $r > R$. In this regard, we consider the following ansatz

$$\langle \psi_{\ell}(r) \rangle = \begin{cases} j_{\ell}^{(d)}(\kappa r) & \text{for } r \leq R, \\ S_{\ell}(k) h_{\ell}^{+(d)}(\kappa r) + h_{\ell}^{-(d)}(\kappa r) & \text{for } r > R, \end{cases} \quad (61)$$

where the generalized spherical Bessel functions are defined by

$$\begin{aligned} h_{\ell}^{\pm(d)}(z) &= \Gamma\left(\frac{d}{2}\right) \left(\frac{2}{z}\right)^{\frac{d-2}{2}} H_{\ell+\frac{d-2}{2}}^{\pm}(z), \\ j_{\ell}^{(d)}(z) &= \frac{h_{\ell}^{+(d)}(z) + h_{\ell}^{-(d)}(z)}{2}, \end{aligned} \quad (62)$$

where $H_{\nu}^{\pm}(z)$ are the Hankel functions [24]. The function $j_{\ell}^{(d)}(z)$ is finite and regular at $z = 0$, hence its presence in the inner region of the ansatz (61). Imposing the continuity condition on the wave function and its derivative at the boundary $r = R$, we quickly get the following expression for the scattering matrix element

$$S_{\ell}(k) = - \frac{W[h_{\ell}^{-(d)}(\kappa r), j_{\ell}^{(d)}(\kappa r)]_{r=R}}{W[h_{\ell}^{+(d)}(\kappa r), j_{\ell}^{(d)}(\kappa r)]_{r=R}}, \quad (63)$$

where $W[f(r), g(r)] = f(r)\partial_r g(r) - g(r)\partial_r f(r)$ denotes the Wronskian with respect to r .

We look for the resonance poles in the scattering matrix element (63) coming from the cancellation of the denominator

$$W[h_{\ell}^{+(d)}(\kappa r), j_{\ell}^{(d)}(\kappa r)]_{r=R} = 0. \quad (64)$$

This equation for $k \in \mathbb{C}$ can be written in terms of the Bessel functions alone as

$$\kappa \frac{J_{\nu+1}(\kappa R)}{J_{\nu}(\kappa R)} = k \frac{H_{\nu+1}^{+}(kR)}{H_{\nu}^{+}(kR)}, \quad (65)$$

where the order ν is given by

$$\nu = \ell + \frac{d - 2}{2}. \quad (66)$$

The comparison between the numerical solutions of Eq. (65) for $k \in \mathbb{C}$ and the actual peaks of the resonance density obtained with MSModel [19] is shown for a 2D point field in Fig. 4(a) and for a three-dimensional (3D) point field in Fig. 4(b). In these two panels, instead of Eq. (20), we exceptionally use the hard-sphere s -wave scattering model given by Eq. (18) of Ref. [18] with the scattering length $\alpha = 0.1 \zeta$. Indeed, this scattering model is more appropriate than Eq. (20) to explore the small- k regime because the cross section does not strongly diverge for $k \rightarrow 0$.

The adequacy between the roots of Eq. (65) and the peaks in Figs. 4(a) and 4(b) shows that, at small values of k , the incident wave mainly perceives the random point field as a semitransparent sphere without the details due to disorder. Moreover, we notice that the peak structure in Figs. 4(a) and 4(b) is very similar to the set of complex resonances of the hard-sphere model shown in Fig. 15 of Appendix A. Why this similarity? In fact, the left-hand side of Eq. (65) is much smoother than the right-hand side and can be approximately treated as a constant. Therefore, the roots of Eq. (65) are located somewhere between the zeros of $H_{\nu}^{+}(kR)$ and those of $H_{\nu+1}^{+}(kR)$. Since each zero of $H_{\nu}^{+}(kR)$ is relatively close to a zero of $H_{\nu+1}^{+}(kR)$, the complete set of roots of Eq. (65) will qualitatively resemble those of

$$H_{\nu}^{+}(kR) = 0, \quad (67)$$

which precisely coincides with the resonance equation (A4) for the hard-sphere model.

However, it should be noted that, in MSModel [19], we used the Green function (13), based on $K_{\nu}(z)$, rather than Eq. (11), based on $H_{\nu}^{+}(z)$, in order to ensure the symmetry (12) with respect the imaginary k axis. This choice places the branch cut on the imaginary axis ($\arg k = -\frac{\pi}{2}$), instead of the real axis ($\arg k = -\pi$), and thus slightly changes the position of the resonances in even dimensions. This explains why the resonance peaks in Fig. 4(a) in the quadrant $\arg k \in [-\pi, -\frac{\pi}{2}]$ do not correspond to the hard-sphere resonances in the same quadrant of Fig. 15. Nothing changes in odd dimension, in Fig. 4(b), because there is no branch cut for $k \in \mathbb{C}$.

It is remarkable that each peak in the resonance densities of Figs. 4(a) and 4(b) can be predicted by the theoretical estimate (65), in spite of the approximations made to get the effective equation (48). In particular, it seems that the number of scatterers does not need to be very large, in contrast to what the Twersky approximation

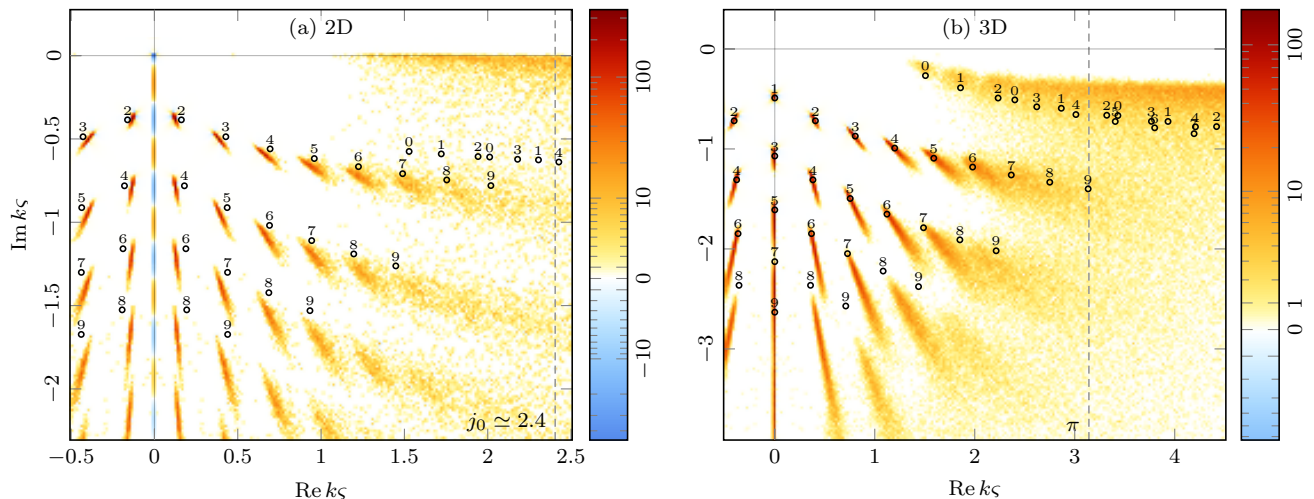


FIG. 4. (a) Resonance density $2\pi\varrho^{(2)}(k_r, k_i)$ computed with MSModel [19] in a 2D disk-shaped random point field for $N = 50$ and using the scattering model given by Eq. (18) of Ref. [18] with $\alpha = 0.1\varsigma$. The density is averaged over 2^8 random configurations. The resonances of the effective medium, obtained by numerically solving Eq. (65), are depicted by small circles labelled with the corresponding angular momentum ℓ . The dashed line separates the low from the high energy region (68). (b) Same as panel (a) but in a 3D ball-shaped random point field for $N = 100$ averaged over 2^8 configurations.

suggested. However, a slight shift between simulation and prediction can be noticed in Fig. 4(a). In addition, the predictions in the upper right side of Fig. 4(a) do not match the resonance band close to the real k axis. These disagreements could be due to Anderson localization because, in 2D, the point cross section is not bounded at low energy due to a logarithmic singularity at $k = 0$. Therefore, the product $k\ell_s = \frac{k}{n\sigma(k)}$ becomes small compared to 1, which thus favors Anderson localization in a finite 2D system [8, 11, 27–30].

On another side, the agreement between the theoretical estimate (65) and the numerical simulation is much more striking in Fig. 4(b). Even better: the theoretical prediction coincides with the faint peaks closest to the real axis for $\ell = 0, 1, 2$ in Fig. 4(b). This is not obvious because these peaks constitute the leftmost edge of the resonance band which was not expected to be described by this theory. At higher energies, however, that is when

$$|k|\varsigma \gtrsim j_{\frac{d-2}{2}}, \quad (68)$$

the prediction (65) does no longer match the position of the resonance band in the upper right side of Fig. 4(b). In order to describe this band, we need to consider a more complete transport theory which remains valid at wavelengths smaller than the mean interscatterer distance ($|k|\varsigma \gtrsim j_{\frac{d-2}{2}}$). This is the subject of Sec. III.

III. SEMICLASSICAL TRANSPORT

In this section, we study the time evolution of a wave packet in the random point field. This study is justified by the fact that the resonances observed in Figs. 4(a)

and 4(b) are intimately connected with the time evolution of a wave packet. In particular, the resonance widths are known to be related to the decay in time of the probability that the particle stays in the medium. Indeed, as far as there is no Anderson localization for trapping the particle, the particle is expected to escape the system at a certain time. In order to investigate this characteristic escape time, it is crucial to consider the time dependence of the square modulus of a wave packet initially located in the medium. As we will see, this approach has the considerable advantage of making the connection with classical mechanics of multiple scattering described by the Boltzmann equation. In particular, when the time t is much larger than the inter-collisional time, the particle is classically expected to enter the diffusive regime for which the envelope of the wave packet obeys the diffusion equation $\partial_t \rho(\mathbf{r}, t) = D \nabla_{\mathbf{r}}^2 \rho(\mathbf{r}, t)$. The quantity of interest is thus the probability density that the particle be at point \mathbf{r} at time t . The main references of this section are the excellent textbooks [7, 8, 16].

Regarding the notations and conventions, we need some adaptations from the previous sections because we did not consider time evolution before. In the framework of the Schrödinger equation, it is convenient to choose the following conventions for the Fourier transform of the pair $f(t) \leftrightarrow \tilde{f}(\omega)$

$$\begin{aligned} \tilde{f}(\omega) &= \int_{\mathbb{R}} e^{+i\omega t} f(t) dt, \\ f(t) &= \frac{1}{2\pi} \int_{\mathbb{R}} e^{-i\omega t} \tilde{f}(\omega) d\omega. \end{aligned} \quad (69)$$

In the same vein, we define the Laplace transform $f(t) \leftrightarrow$

$\check{f}(s)$ as

$$\begin{aligned}\check{f}(s) &= \int_0^\infty e^{-st} f(t) dt, \\ f(t) &= \frac{1}{2\pi i} \int_{-i\infty}^{i\infty} e^{st} \check{f}(s) ds.\end{aligned}\quad (70)$$

Throughout this section, we assume $\hbar = 2m = 1$ for convenience, so that the energy is also denoted as $E = \hbar\omega = \omega$, the energy-momentum relation becomes $\omega = k^2$, and the group velocity reads $v = 2k$.

A. Time evolution of a wave packet

1. Creation of the wave packet

We want to define the probability density, $\rho(\mathbf{r}, t)$, that the particle be located at point \mathbf{r} after a time t given it started at $t = 0$ from position \mathbf{r}_0 with a certain energy. Unfortunately, this task does not seem feasible in stationary quantum mechanics because of the non-trivial initial condition at \mathbf{r}_0 . Indeed, a quantum state cannot simultaneously have a well-defined energy and no spatial extent due to the uncertainty principle. To address this issue, a compromise must be found between the spatial extent and the spectral width of the initial state. A relatively neat way of doing this is to manually create a wave packet of central frequency ω_0 around time $t = 0$ during the time window Δt at the center of the system. This can be done with the formal time-dependent Schrödinger equation¹ for the particle state $|\psi(t)\rangle$

$$i \frac{d}{dt} |\psi(t)\rangle = \hat{H} |\psi(t)\rangle + S(t) |\psi_0\rangle, \quad (71)$$

where \hat{H} is the Hamiltonian of the complete multiple-scattering problem. We assume that the initial condition is $|\psi(t)\rangle = 0$ for $t \rightarrow -\infty$. In Eq. (71), $S(t) |\psi_0\rangle$ is a source term which creates a particle of central frequency ω_0 in state $|\psi_0\rangle$ around time $t = 0$. We assume the following expression for the source term

$$\begin{aligned}S(t) &= e^{-\frac{t^2}{2(\Delta t)^2}} e^{-i\omega_0 t}, \\ \tilde{S}(\omega) &= \sqrt{2\pi}\Delta t e^{-(\omega-\omega_0)^2(\Delta t)^2/2}.\end{aligned}\quad (72)$$

The duration Δt of this input signal is supposed to be much longer than the central oscillation period $2\pi/\omega_0$. Note that, in the special case of a infinite time window ($\Delta t \rightarrow \infty$), the functions in Eq. (72) reduce to

$S(t) = e^{-i\omega_0 t}$ and $\tilde{S}(\omega) = 2\pi\delta(\omega - \omega_0)$. In that extreme case, the wave function becomes stationary and the probability density does not depend on time. Regarding the state $|\psi_0\rangle$ in Eq. (71), we will typically take a position eigenstate, $|\psi_0\rangle = |\mathbf{r}_0\rangle$, although this restriction is not necessary for the moment. The formal Schrödinger equation (71) can be solved under the Fourier transform in time (69). The result is

$$|\psi(t)\rangle = \frac{1}{2\pi} \int_{\mathbb{R}} e^{-i\omega t} \tilde{S}(\omega) \hat{Q}(\omega_+) |\psi_0\rangle d\omega, \quad (73)$$

where $\hat{Q}(\omega)$ is the resolvent of the full problem

$$\hat{Q}(\omega) = \frac{1}{\omega - \hat{H}} \quad \forall \omega \in \mathbb{C} \setminus \mathbb{R}^+, \quad (74)$$

and ω_{\pm} is a notation for $\omega \pm i\varepsilon$ in the limit $\varepsilon \xrightarrow{\sim} 0$. This complex shift is required for the proper convergence of integral (73). Note that, in Eq. (74), the argument of the resolvent is the frequency and not the wavenumber as before.

2. Time evolution of the density matrix

An even more useful quantity than the probability density $\rho(\mathbf{r}, t)$ is the *density matrix* defined for a pure state $|\psi(t)\rangle$ by

$$\hat{\rho}(t) = |\psi(t)\rangle \langle \psi(t)|. \quad (75)$$

This matrix contains much more information about the particle state than the probability distribution alone, especially the momentum, the direction of motion and the coherence, given by its off-diagonal elements. Moreover, the probability density is just the diagonal part of the density matrix: $\rho(\mathbf{r}, t) = \langle \mathbf{r} | \hat{\rho}(t) | \mathbf{r} \rangle$. Instead of calculating $\hat{\rho}(t)$ as a time-dependent function, inserting directly Eq. (73) into Eq. (75), it turns out to be more convenient to determine the Laplace transform of $\hat{\rho}(t)$ in time

$$\hat{\rho}(s) = \int_0^\infty e^{-st} \hat{\rho}(t) dt. \quad (76)$$

Another way is to use the Fourier transform of $\hat{\rho}(t)$, as usually done in the literature [7, 8]. However, we find the Laplace transform more suitable than the Fourier transform for non-oscillating signals such as the diagonal part of $\hat{\rho}(t)$.

The advantage of $\hat{\rho}(s)$ in Eq. (76) is that, in contrast to $|\psi(t)\rangle$, it does not explicitly depend on time. The information contained in $\hat{\rho}(s)$ is just equivalent to the information in $\hat{\rho}(t)$, except that the interpretation is not the same. Furthermore, since we consider periods of time well after the particle has been created, we have $t \gg \Delta t$. The dual relationship is $s \ll \frac{1}{\Delta t}$ under the Laplace transform. This means that the Laplace variable, s , must be much smaller than the bandwidth, $\frac{1}{\Delta t}$, of the particle.

¹ Note that time-dependent Schrödinger equations with source terms are generally reserved for electromagnetism to describe the creation or absorption of photons. However, it is not physically justified for matter particles. Here, the use of this equation is only motivated by the convenience of the formalism to specify the temporal characteristics of the wave packet.

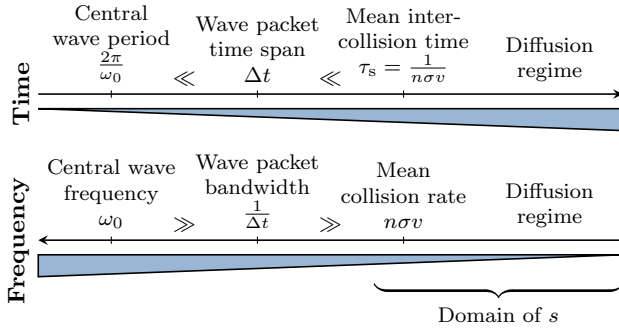


FIG. 5. Hierarchy of characteristic times and frequencies involved in the evolution of a quantum wave packet in a random medium in the weak scattering regime.

The main characteristic time scales of this system are summarized in Fig. 5.

An important corollary of the assumption that the frequency is much larger than the collision rate ($\omega_0 \gg n\sigma v$) is that the wavelength is much smaller than the mean free path²

$$k_0 \ell_s \gg 1. \quad (77)$$

This is indeed equivalent to $\omega_0 \gg n\sigma v$ as long as the dispersion relation is a power law: $\omega(k) \propto k^\alpha \forall \alpha > 0$. The condition (77) is known in the literature as the *weak scattering regime* [8], or the *weak disorder regime* [7]. In this regime, the localization effects play less significant roles, especially in 2D and 3D. Note that, in the context of gaseous particle detectors, the condition (77) is usually met. In this regard, some orders of magnitude are shown in Tab. I. Therefore, we find reasonable to neglect these

Particle	k_0	ℓ_s	$k_0 \ell_s$
Electron, 10 eV [31, 32]	16 nm^{-1}	$0.4 \mu\text{m}$	6×10^3
Alpha, 5 MeV [33]	1 fm^{-1}	$1 \mu\text{m}$	1×10^9
Photon, 550 nm [34]	$11 \mu\text{m}^{-1}$	100 km	1×10^{12}

TABLE I. Orders of magnitude for the wavenumber and the mean free path of some particles in dry ambient air ($P = 10^5 \text{ Pa}$ and $T = 273 \text{ K}$). The molecular density is $n = 0.0265 \text{ nm}^{-3}$. The visible light data only assumes the Rayleigh scattering.

effects in this section.

Now, substituting Eq. (73) into Eq. (76), we get

$$\hat{\rho}(s) = \int_{\mathbb{R}^2} \frac{d\omega d\omega'}{(2\pi)^2} \int_0^\infty dt e^{-(s+i\omega-i\omega')t} \times \tilde{S}(\omega) \tilde{S}^*(\omega') \hat{Q}(\omega_+) \hat{\rho}_0 \hat{Q}(\omega_-), \quad (78)$$

where $\hat{\rho}_0$ denotes the density matrix associated with the initial state

$$\hat{\rho}_0 = |\psi_0\rangle \langle \psi_0|. \quad (79)$$

Integrating over the time t , Eq. (78) becomes

$$\hat{\rho}(s) = \int_{\mathbb{R}^2} \frac{d\omega d\omega'}{(2\pi)^2} \frac{\tilde{S}(\omega) \tilde{S}^*(\omega')}{s + i(\omega - \omega')} \hat{Q}(\omega_+) \hat{\rho}_0 \hat{Q}(\omega_-), \quad (80)$$

Regarding the double integral over the frequencies, we consider the following change of variable

$$\begin{cases} \omega_m = \frac{1}{2}(\omega + \omega'), \\ \omega_d = \omega - \omega', \end{cases} \quad \begin{cases} \omega = \omega_m + \frac{1}{2}\omega_d, \\ \omega' = \omega_m - \frac{1}{2}\omega_d. \end{cases} \quad (81)$$

The change of variable (81) turns the integral (80) into

$$\begin{aligned} \hat{\rho}(s) = \int_{\mathbb{R}^2} \frac{d\omega_m d\omega_d}{(2\pi)^2} \frac{\tilde{S}(\omega_m + \frac{\omega_d}{2}) \tilde{S}^*(\omega_m - \frac{\omega_d}{2})}{s + i\omega_d} \\ \times \hat{Q}(\omega_m + \frac{\omega_d}{2}) \hat{\rho}_0 \hat{Q}(\omega_m - \frac{\omega_d}{2}). \end{aligned} \quad (82)$$

In this way, the frequency difference, ω_d , can be integrated out with the residue theorem around the simple pole at $\omega_d = is$. The result is

$$\begin{aligned} \hat{\rho}(s) = \int_{\mathbb{R}} \frac{d\omega_m}{2\pi} \tilde{S}(\omega_m + \frac{is}{2}) \tilde{S}^*(\omega_m - \frac{is}{2}) \\ \times \hat{Q}(\omega_m + \frac{is}{2}) \hat{\rho}_0 \hat{Q}(\omega_m - \frac{is}{2}). \end{aligned} \quad (83)$$

To perform the remaining integral over the central frequency ω_m , we need to go back to the window function (72). Since the time span of the window is supposed to be much larger than the central wave period, i.e., $\Delta t \gg \omega_0^{-1}$, we can approximate the spectral power of the source by a Dirac delta over the frequencies

$$\begin{aligned} \tilde{S}(\omega_m + \frac{is}{2}) \tilde{S}^*(\omega_m - \frac{is}{2}) = 2\pi(\Delta t)^2 e^{-(\omega_m - \omega_0 + \frac{is}{2})^2 (\Delta t)^2} \\ \xrightarrow{\Delta t \gg \omega_0^{-1}} 2\pi M(s) \delta(\omega_m - \omega_0), \end{aligned} \quad (84)$$

where $M(s)$ denotes the function

$$M(s) = \sqrt{\pi} \Delta t e^{s^2 (\Delta t)^2 / 4}. \quad (85)$$

As explained before, the Laplace variable s is supposed to be much smaller than the spectral bandwidth $(\Delta t)^{-1}$ of the wave packet. Therefore, the function $M(s)$ in Eqs. (85) and (84) can reasonably be approximated by $M(0)$. In addition, for the sake of simplicity, we decide to absorb the constant factor $M(0)$ in the normalization of the initial state $\hat{\rho}_0$. Anyway, the question of the normalization of $\hat{\rho}(s)$ will be addressed later. Finally, using Eq. (84), the density matrix (83) reduces to

$$\hat{\rho}(s) = \hat{Q}(\omega_0 + \frac{is}{2}) \hat{\rho}_0 \hat{Q}(\omega_0 - \frac{is}{2}). \quad (86)$$

This is the sought expression for the Laplace transform of the density matrix. We notice on Eq. (86) the other

² Note that, since the mean free path is at least equal to the mean interatomic distance ($\ell_s = \varsigma$), the condition (77) is necessarily satisfied for $k_0 \varsigma \gg 1$.

advantage of the Laplace transform on the usual Fourier transform [7, 8]. Indeed, the right-hand Green function in Eq. (86) is just the Hermitian conjugate of the left-hand Green function, according to $\hat{Q}^\dagger(\omega) = \hat{Q}(\omega^*)$. Therefore, the Green functions are only evaluated at the single energy value $\omega_+ = \omega_0 + \frac{i}{2}s$. If we had calculated the Fourier transform, s would have been imaginary, leading to two different real energies in Eq. (86), and thus less convenient expressions. This shows the interest of the Laplace transform in this context.

The density matrix (86) is likely more transparent when expressed in position space. If we assume that the particle initially starts in the position eigenstate $\hat{\rho}_0 = |\mathbf{r}_0\rangle\langle\mathbf{r}_0|$, then the density matrix reads [7, 8]

$$\langle\mathbf{r}|\hat{\rho}(s)|\mathbf{r}'\rangle = Q(k_+, \mathbf{r}|\mathbf{r}_0)Q^*(k_+, \mathbf{r}'|\mathbf{r}_0), \quad (87)$$

where the wavenumbers k_\pm corresponding to the frequencies $\omega_\pm = \omega_0 \pm \frac{i}{2}s$ in Eq. (86) are given by

$$k_\pm = k_0 \pm i\frac{s}{2v}, \quad (88)$$

for the group velocity v . This also shows that $s = \gamma v$ according to the notation (54). Note again that Eq. (87) does not explicitly depend on k_- , since $k_- = k_+^*$. The result (87) confirms the physical usefulness of having considered complex wavenumbers since the beginning of this work. In particular, the complex nature of the wavenumber will play a crucial role in the interpretation of the resonance band in Sec. III G.

3. Normalization of the density matrix

Now, we verify that the normalization of the wave packet is conserved in time. This must be the case because, after its creation at time $t = 0$, the wave packet does not undergo absorption in our model. The purpose of the following calculation is twofold: showing that the total probability is conserved after time $t = 0$, but also finding the normalization constant. The total probability in the density matrix $\text{Tr} \hat{\rho}(s)$ is given by its trace. Thus, using Eq. (86), we need to find

$$\text{Tr} \hat{\rho}(s) = \text{Tr} [\hat{Q}(\omega_+) \hat{\rho}_0 \hat{Q}(\omega_-)], \quad (89)$$

where $\omega_\pm = \omega_0 \pm \frac{i}{2}s$. The resolvents in Eq. (89) can be put next to each other in virtue of the cyclic property of trace $\text{Tr}(\hat{A}\hat{B}\hat{C}) = \text{Tr}(\hat{B}\hat{C}\hat{A})$, which holds for trace-class operators. Then, their product is decomposed using the first resolvent identity [35]

$$\hat{Q}(\omega_-)\hat{Q}(\omega_+) = -\frac{\hat{Q}(\omega_+) - \hat{Q}(\omega_-)}{\omega_+ - \omega_-}. \quad (90)$$

Since the Laplace variable s is supposed to be much smaller than the central frequency of the wave packet (see Fig. 5), Eq. (90) gets simplified in

$$\hat{Q}(\omega_-)\hat{Q}(\omega_+) \xrightarrow{s \ll \omega_0} \frac{2\pi}{s} \delta(\omega_0 - \hat{H}), \quad (91)$$

where \hat{H} denotes the Hamiltonian of the full system, possibly with a random potential. Therefore, Eq. (89) becomes

$$\text{Tr} \hat{\rho}(s) = \frac{2\pi}{s} \text{Tr} \left[\underbrace{\delta(\omega_0 - \hat{H})}_{\mu(\omega_0|\hat{\rho}_0)} \hat{\rho}_0 \right], \quad (92)$$

We identify the remaining trace in the right-hand side of Eq. (92) as the local density of states $\mu(\omega_0|\hat{\rho}_0)$ in the initial state $\hat{\rho}_0$. This factor is just a time independent constant because it does not depend on s . Finally, the time evolution of the trace of the density matrix can be obtained through inverse Laplace transform

$$\begin{aligned} \text{Tr} \hat{\rho}(t) &= \frac{1}{2\pi i} \int_{-i\infty}^{i\infty} e^{st} \frac{2\pi}{s} \mu(\omega_0|\hat{\rho}_0) ds \\ &= 2\pi \mu(\omega_0|\hat{\rho}_0) \Theta(t), \end{aligned} \quad (93)$$

where $\Theta(t)$ denotes the Heaviside step function:

$$\Theta(t) = \begin{cases} 0 & t < 0, \\ 1 & t \geq 0. \end{cases} \quad (94)$$

The result (93) confirms that the probability is indeed conserved since the creation of the particle at time $t = 0$, as expected. It also gives us the normalization constant of the density matrix (86), which is just $2\pi\mu(\omega_0|\hat{\rho}_0)$ [7].

4. Propagation in free space

In addition to the normalization, we may verify the consistency of the density matrix (87) in the special case of a freely propagating wave packet created at the point \mathbf{r}_0 around time $t = 0$. In this case, the Green function reduces to the free-space Green function (13). Thus, we have

$$\langle\mathbf{r}|\hat{\rho}(s)|\mathbf{r}'\rangle = G(k_+, r)G^*(k_+, r'), \quad (95)$$

where $r = \|\mathbf{r} - \mathbf{r}_0\|$ and $r' = \|\mathbf{r}' - \mathbf{r}_0\|$, and the wavenumber is $k_+ = k_0 + i\frac{s}{2v}$ according to Eq. (88). At large enough distance, the Green function can be approached by the asymptotic behavior (14). Therefore, the evanescent effect of the imaginary part of k_+ can be factored out as

$$\langle\mathbf{r}|\hat{\rho}(s)|\mathbf{r}'\rangle \simeq G(k_0, r)G^*(k_0, r') e^{-\frac{s}{2v}(r+r')}. \quad (96)$$

The time dependence can then be restored by inverse Laplace transform, turning the decreasing exponential into a Dirac delta

$$\langle\mathbf{r}|\hat{\rho}(t)|\mathbf{r}'\rangle = G(k_0, r)G^*(k_0, r')\delta(t - \frac{r+r'}{2v}). \quad (97)$$

In particular, the probability density can be found on the diagonal of the density matrix, that is to say

$$\rho(\mathbf{r}, t) = |G(k_0, r)|^2 \delta(t - \frac{r}{v}). \quad (98)$$

Finally, the Green function in Eq. (98) can be eliminated using Eq. (14) and $v = 2k_0$. One finds [7]

$$\rho(\mathbf{r}, t) = \frac{2\pi\mu_0(\omega_0 | \mathbf{r}_0)}{S_d r^{d-1}} \delta(r - vt), \quad (99)$$

where $\mu_0(\omega_0 | \mathbf{r}_0)$ is the free-space local density of states given by Eq. (18) with $k_0 = \sqrt{\omega_0}$. The result (99) can be interpreted as a spherical distribution propagating in all directions at speed v . In the absence of collision with the scatterers, the free motion of the wave packet continues forever from time $t = 0$. The conservation of probability is ensured by the factor $S_d r^{d-1}$ which is just the surface of the spherical distribution. Equation (99) is also consistent with the normalization factor $2\pi\mu(\omega_0 | \hat{\rho}_0)$ previously found in Eq. (93), hence confirming the validity of our calculation.

B. Derivation of the semiclassical transport equation

In this section, we derive the transport equation for the average density matrix $\langle \hat{\rho}(s) \rangle$ in the random point field using the diagrammatic approach of Ref. [16]. For this purpose, let us look closer at the density matrix $\hat{\rho}(s)$ from Eq. (86) when we substitute the propagator $\hat{Q}(k)$ for the multiple-scattering expansion (41)

$$\begin{aligned} \hat{Q}(k)\hat{\rho}_0\hat{Q}^\dagger(k) &= \sum_{p=0}^{\infty} \sum_{i_1, \dots, i_p} \sum_{q=0}^{\infty} \sum_{i'_1, \dots, i'_q} \hat{G}\hat{F}_{i_p}\hat{G} \dots \hat{G}\hat{F}_{i_1}\hat{G}\hat{\rho}_0 \\ &\quad \times \hat{G}^\dagger\hat{F}_{i'_1}^\dagger\hat{G}^\dagger \dots \hat{G}^\dagger\hat{F}_{i'_q}^\dagger\hat{G}^\dagger. \end{aligned} \quad (100)$$

Note that the wavenumber is implicitly complex $k = k_+ = k_0 + \frac{i}{2}\gamma$ with $\gamma = s/v$. Note also that the sums over the paths $\mathcal{P} = (i_1, \dots, i_p)$ and $\mathcal{Q} = (i'_1, \dots, i'_q)$ in Eq. (100) are completely independent of each other, meaning that the indices are allowed to coincide. To remain consistent with the approximations we made in Sec. II B, we assume that the number of scatterers is large enough so that the Twersky approximation holds. In other words, we assume that the paths \mathcal{P} and \mathcal{Q} involved in Eq. (100) are both self-avoiding. However, this does not prevent some indices of \mathcal{P} to be equal to indices of \mathcal{Q} .

The diagrams of some low-order terms of Eq. (100) are shown in Fig. 6 using the notations of Fig. 1(a). To make things easier to read, it is more convenient to fold the diagrams in half around the initial state $\hat{\rho}_0$, as done in the modern literature [7, 8, 15, 16]. The initial state $\hat{\rho}_0$ itself is represented by a black dot on the right side. In this way, the sequence of collisions should be chronologically read from right to left, as it was the case in Fig. 1(b). As one can see, the diagrams with links in the upper branch or in the lower branch have already been excluded from Fig. 6 according to the Twersky approximation, such as

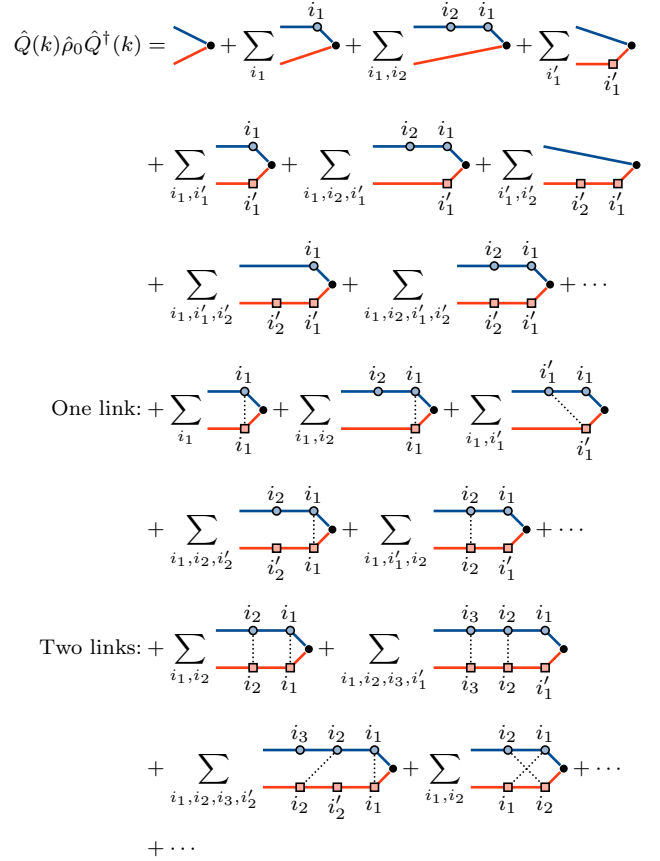


FIG. 6. Expansion of the density matrix $\hat{\rho}(s)$ from Eq. (100) under the Twersky approximation using the notations of Fig. 1(a). The black dots represent the initial state $\hat{\rho}_0$. The list of diagrams is not exhaustive. The sums implicitly assume that the indices i_1, i_2, \dots are different from each other.

in Fig. 1(b). The only allowed diagrams with links connect the upper and lower branches. Note also that one scattering site cannot have more than one link again because of the Twersky approximation. Indeed, that would mean that one would have internal links in the other branch.

With all these rules in mind, we are able to expand the configurational average of Eq. (100) further. Let us first consider the diagrams with no link shown in the first three lines of Fig. 6. Since then all the scatterers are assumed to be different, the configurational average applies separately to each branch, and we can write

$$\begin{aligned} \langle \hat{Q}(k)\hat{\rho}_0\hat{Q}^\dagger(k) \rangle_0 &= \left\langle \sum_{p=0}^{\infty} \sum_{i_1, \dots, i_p} \hat{G}\hat{F}_{i_p}\hat{G} \dots \hat{G}\hat{F}_{i_1}\hat{G} \right\rangle \hat{\rho}_0 \\ &\quad \times \left\langle \sum_{q=0}^{\infty} \sum_{i'_1, \dots, i'_q} \hat{G}^\dagger\hat{F}_{i'_1}^\dagger\hat{G}^\dagger \dots \hat{G}^\dagger\hat{F}_{i'_q}^\dagger\hat{G}^\dagger \right\rangle. \end{aligned} \quad (101)$$

The zero subscript of $\langle \cdot \rangle_0$ refers to the absence of link between the two branches. Note that the sums in Eq. (101)

implicitly assume that no index of the first path \mathcal{P} can be equal to any of the indices of the second path \mathcal{Q} . Now, we notice that each of the two branches in Eq. (101) is given by the average of the full propagator (41). Therefore, Eq. (101) is equivalent to

$$\langle \hat{Q}(k) \hat{\rho}_0 \hat{Q}^\dagger(k) \rangle_0 = \langle \hat{Q} \rangle \hat{\rho}_0 \langle \hat{Q}^\dagger \rangle, \quad (102)$$

which can be easily interpreted as the average of a product of independent random variables.

Then, we consider the diagrams with a single link, partially shown in the third line of Fig. 6. One way to treat them is to fix the scatterer involved in the link, say \mathbf{x}_i , and to split the paths \mathcal{P} and \mathcal{Q} in two around this point [5, 15]. Thus, we have more explicitly

$$\begin{cases} \mathcal{P} = (\mathcal{P}_1, i, \mathcal{P}_2) = (i_1, i_2, \dots, i_{p_1}, i, j_1, j_2, \dots, j_{p_2}), \\ \mathcal{Q} = (\mathcal{Q}_1, i, \mathcal{Q}_2) = (i'_1, i'_2, \dots, i'_{q_1}, i, j'_1, j'_2, \dots, j'_{q_2}). \end{cases} \quad (103)$$

Given the Twersky approximation, no other indices than i are allowed to coincide. The index i itself must be unique. Using the paths (103), the terms with one link in Eq. (100) can be gathered as

$$\begin{aligned} \langle \hat{Q}(k) \hat{\rho}_0 \hat{Q}^\dagger(k) \rangle_1 &= \left\langle \sum_i \left(\sum_{\mathcal{P}_1, \mathcal{P}_2} \hat{G}_{\mathcal{P}_1} \hat{F}_i \hat{G}_{\mathcal{P}_2} \right) \hat{\rho}_0 \right. \\ &\quad \times \left. \left(\sum_{\mathcal{Q}_1, \mathcal{Q}_2} \hat{G}_{\mathcal{Q}_1}^\dagger \hat{F}_i^\dagger \hat{G}_{\mathcal{Q}_2}^\dagger \right) \right\rangle, \end{aligned} \quad (104)$$

where the notation $\hat{G}_{\mathcal{P}}$ stands for the product

$$\hat{G}_{\mathcal{P}} = \hat{G}_{\hat{F}_{i_p}} \hat{G} \cdots \hat{G}_{\hat{F}_{i_2}} \hat{G}_{\hat{F}_{i_1}} \hat{G}. \quad (105)$$

Again, the subscript of $\langle \cdot \rangle_1$ in Eq. (104) recalls that the diagrams contain only one link. Since all the points in $\mathcal{P}_1, \mathcal{P}_2, \mathcal{Q}_1$ and \mathcal{Q}_2 are statistically independent, the configurational average applies to each of them separately. They all yield the effective propagator

$$\left\langle \sum_{\mathcal{P}} \hat{G}_{\mathcal{P}} \right\rangle = \langle \hat{Q} \rangle, \quad (106)$$

according to Eqs. (41) and (105). In the end, only the terms \hat{F}_i and \hat{F}_i^\dagger remain because they are obviously not independent. We can now release the previously fixed scatterer \mathbf{x}_i , and average it in space. The result reads

$$\begin{aligned} \langle \hat{Q}(k) \hat{\rho}_0 \hat{Q}^\dagger(k) \rangle_1 &= \int_{\mathbb{R}^d} \langle \hat{Q} \rangle \hat{F}_{\mathbf{x}} \langle \hat{Q} \rangle \hat{\rho}_0 \\ &\quad \times \langle \hat{Q}^\dagger \rangle \hat{F}_{\mathbf{x}}^\dagger \langle \hat{Q}^\dagger \rangle n(\mathbf{x}) d\mathbf{x}. \end{aligned} \quad (107)$$

where $\hat{F}_{\mathbf{x}} = F(k) |\mathbf{x}\rangle \langle \mathbf{x}|$.

From these calculations, we can guess the general procedure to determine the contribution from diagrams with more links. This can be summarized in three steps.

- First, fixing the scatterers involved in the links,
- then averaging over the independent paths, leading to factors $\langle \hat{Q} \rangle$,
- and, finally, averaging over the previously fixed scatterers.

In particular, the second step is illustrated in Fig. 7. In

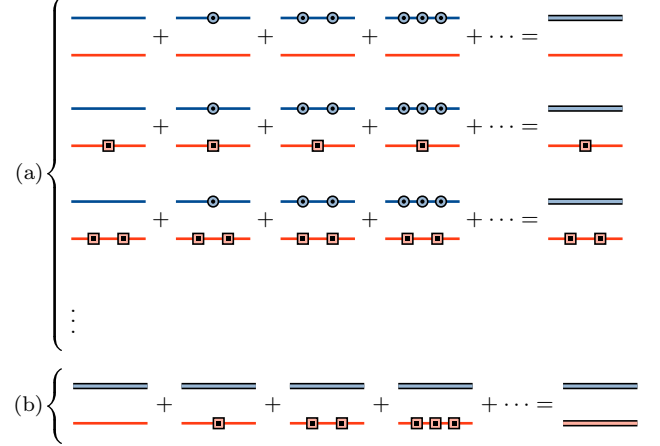
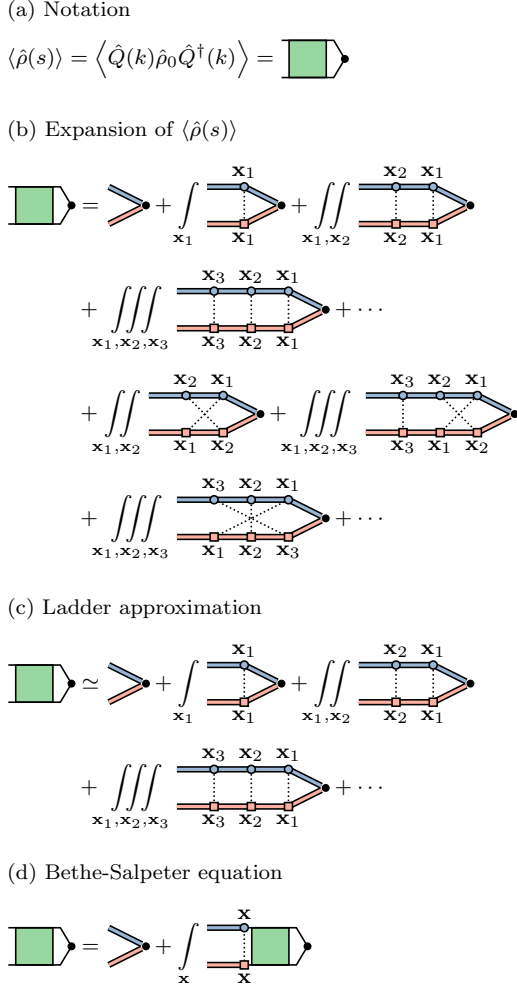


FIG. 7. Resummation of the diagrams with no link for the average density matrix $\langle \hat{\rho}(s) \rangle$. (a) Individual resummation of diagrams with fixed number of vertices in the lower arm. (b) Final resummation of all the contributions from panel (a).

fact, between any fixed scatterers, we may have an arbitrary number of collisions, which, on average, leads to the effective propagator $\langle \hat{Q} \rangle$. Therefore, everything is going *as if* \hat{G} is simply replaced by $\langle \hat{Q} \rangle$ upon averaging. Finally, only links remain visible. For instance, the diagrams with two links, including those in the last two lines of Fig. 6, can also be summed up in this way. However, we must be careful that the links may cross each other. This leads to two separate kinds of terms whose resummation reads

$$\begin{aligned} \langle \hat{\rho} \rangle_2 &= \iint_{\mathbb{R}^{2d}} \langle \hat{Q} \rangle \hat{F}_{\mathbf{x}_2} \langle \hat{Q} \rangle \hat{F}_{\mathbf{x}_1} \langle \hat{Q} \rangle \hat{\rho}_0 \\ &\quad \times \langle \hat{Q}^\dagger \rangle \hat{F}_{\mathbf{x}_1}^\dagger \langle \hat{Q}^\dagger \rangle \hat{F}_{\mathbf{x}_2}^\dagger \langle \hat{Q}^\dagger \rangle n(\mathbf{x}_1) n(\mathbf{x}_2) d\mathbf{x}_1 d\mathbf{x}_2 \\ &\quad + \iint_{\mathbb{R}^{2d}} \langle \hat{Q} \rangle \hat{F}_{\mathbf{x}_2} \langle \hat{Q} \rangle \hat{F}_{\mathbf{x}_1} \langle \hat{Q} \rangle \hat{\rho}_0 \\ &\quad \times \langle \hat{Q}^\dagger \rangle \hat{F}_{\mathbf{x}_2}^\dagger \langle \hat{Q}^\dagger \rangle \hat{F}_{\mathbf{x}_1}^\dagger \langle \hat{Q}^\dagger \rangle n(\mathbf{x}_1) n(\mathbf{x}_2) d\mathbf{x}_1 d\mathbf{x}_2. \end{aligned} \quad (108)$$

Note the order of indices of $\hat{F}_{\mathbf{x}_1}$ and $\hat{F}_{\mathbf{x}_2}$ in these two terms. The new expansion of $\langle \hat{\rho}(s) \rangle$ is graphically represented in Fig. 8(b) using the symbol in Fig. 8(a). The upper and lower legs of the symbol in Fig. 8(a) depicts the left and right inputs of the operator $\langle \hat{\rho}(s) \rangle$, respectively. As one can see, Fig. 8(b) is very similar to Fig. 6, except that the unlinked scatterers are omitted and replaced by the effective propagator $\langle \hat{Q} \rangle$ or $\langle \hat{Q}^\dagger \rangle$. This is a consequence of the resummation illustrated in Fig. 7.



wavenumber k . In the weak scattering regime ($|\kappa| \simeq |k|$), one finds from Eq. (55)

$$K(\mathbf{r} | \mathbf{r}') \xrightarrow{r \rightarrow \infty} \frac{e^{-(\gamma+n\sigma)\|\mathbf{r}-\mathbf{r}'\|}}{S_d \|\mathbf{r}-\mathbf{r}'\|^{d-1}}, \quad (113)$$

where $\gamma = \frac{s}{v} = 2\text{Im}k$ is the dual variable of time under Laplace transform.

Using the kernel (112) and the point cross section formula (19), the diagonal part of Eq. (110) reads

$$\langle \rho(\mathbf{r}) \rangle = K(\mathbf{r} | \mathbf{r}_0) + \int_{\mathbb{R}^d} K(\mathbf{r} | \mathbf{r}') n(\mathbf{r}') \sigma(k) \langle \rho(\mathbf{r}') \rangle d\mathbf{r}'. \quad (114)$$

Note that the small imaginary part of $k = k_0 + ik_i$ can be neglected in the cross section because the equation only considers time scales much longer than the oscillation period of the wave ($s \ll \omega_0$ and $k_i \ll k_0$). It is thus safe to write $\sigma(k) \simeq \sigma(k_0)$. Note also that, from Eq. (110) to Eq. (114), we have slightly changed the normalization of the density because the source term $|\langle Q(k, \mathbf{r} | \mathbf{r}_0) \rangle|^2$ became $K(\mathbf{r} | \mathbf{r}_0)$. However, this has no consequence on $\langle \rho(\mathbf{r}) \rangle$ except for an irrelevant global factor.

One ultimately obtains the self-consistent equation (114) for the average probability density $\langle |\psi(\mathbf{r})|^2 \rangle$ alone. Equation (114) describes the multiple scattering of the particle, of density $\langle \rho(\mathbf{r}) \rangle$, in the medium. The last term of the right-hand side accounts for the individual collisions which may occur anywhere in the medium, hence the integral over \mathbf{r}' . The integral kernel $K(\mathbf{r} | \mathbf{r}')$ can be interpreted as the probability density for the next collision point \mathbf{r} given the previous collision happened at \mathbf{r}' .

C. Relationship with the linear Boltzmann equation

In this section, we show that the integral transport equation (114) is consistent with the famous linear Boltzmann equation [7, 12, 42]

$$\begin{aligned} & \frac{\partial f}{\partial t} + v\boldsymbol{\Omega} \cdot \nabla_{\mathbf{r}} f \\ &= nv \oint_{S_d} d\Omega' \frac{d\sigma}{d\Omega}(\boldsymbol{\Omega} | \boldsymbol{\Omega}') (f(\mathbf{r}, \boldsymbol{\Omega}', t) - f(\mathbf{r}, \boldsymbol{\Omega}, t)), \end{aligned} \quad (115)$$

where $\frac{d\sigma}{d\Omega}$ is the differential cross section of a point scatterer, and $f(\mathbf{r}, \boldsymbol{\Omega}, t)$ is the distribution function of a classical particle in the phase space, \mathbf{r} being the position, and $\boldsymbol{\Omega}$ the direction of motion.

The function $f(\mathbf{r}, \boldsymbol{\Omega}, t)$ is closely related to the Wigner function of the wave function $\psi(\mathbf{r}, t)$ averaged over the random configurations of the disorder. As shown in Ref. [22], under certain assumptions, the Wigner function of a quantum particle evolving in a gas of moving quantum particles obeys the linear Boltzmann equation (115).

In particular, this equation remains valid when the quantum particles are stopped in space. In this case, the partial trace over the quantum environment, which must be achieved to determine the density matrix of the particle, is completely equivalent to the average over the random configurations of the point field, Eq. (4), involved in this paper.

The loss term in the right-hand side of Eq. (115) can be exactly evaluated, since $f(\mathbf{r}, \boldsymbol{\Omega}, t)$ does not depend on the integrated direction $\boldsymbol{\Omega}'$. This integral lets appear the total cross section σ . Putting this term in the left-hand side, we get

$$\begin{aligned} & \left(\frac{\partial}{\partial t} + v\boldsymbol{\Omega} \cdot \nabla_{\mathbf{r}} + n\sigma v \right) f \\ &= nv \oint_{S_d} d\Omega' \frac{d\sigma}{d\Omega}(\boldsymbol{\Omega} | \boldsymbol{\Omega}') f(\mathbf{r}, \boldsymbol{\Omega}', t). \end{aligned} \quad (116)$$

We want to derive an integral transport equation which does not depend anymore on the particle direction of motion $\boldsymbol{\Omega}$. To this end, we will use the Green function method. We interpret the brackets in the left-hand side of Eq. (116) as a linear operator acting on f to be inverted. Thus, we consider the integral kernel given by the equation

$$\begin{aligned} & \left(\frac{\partial}{\partial t} + v\boldsymbol{\Omega} \cdot \nabla_{\mathbf{r}} + n\sigma v \right) K(\mathbf{r}, \boldsymbol{\Omega}, t | \mathbf{r}', \boldsymbol{\Omega}', t') \\ &= \delta(\mathbf{r} - \mathbf{r}') \delta(\boldsymbol{\Omega} - \boldsymbol{\Omega}') \delta(t - t'). \end{aligned} \quad (117)$$

The function K is generally referred to as the transport kernel [42]. The solution of Eq. (117) reads

$$\begin{aligned} & K(\mathbf{r}, \boldsymbol{\Omega}, t | \mathbf{r}', \boldsymbol{\Omega}', t') \\ &= e^{-n\sigma\|\mathbf{r}-\mathbf{r}'\|} \delta(\mathbf{r} - \mathbf{r}' - v\boldsymbol{\Omega}(t - t')) \delta(\boldsymbol{\Omega} - \boldsymbol{\Omega}'). \end{aligned} \quad (118)$$

Note that this kernel is supposed to be identically zero for $t < t'$. This can be realized with a Heaviside step function $\Theta(t - t')$, but we leave it implicit.

The function (118) can be interpreted as the distribution of a particle located at $\mathbf{r} = \mathbf{r}' + v\boldsymbol{\Omega}(t - t')$ for $t \geq t'$ in position space and $\boldsymbol{\Omega} = \boldsymbol{\Omega}'$ in direction space. This is the probability distribution that the particle does not undergo any collision after distance $\|\mathbf{r} - \mathbf{r}'\|$ from the previous collision at \mathbf{r}' [7]. The exponential prefactor comes from the constant collision rate $n\sigma v$ in the left-hand side of Eq. (117). Since the collisions constitute a Poisson process and are less and less unavoidable over time, this probability exponentially vanishes. In some way, this decay can be understood as the absorption of the particle in a collision event. The particle is then recreated by the gain term in the right-hand side of Eq. (117). Of course, this is a strictly mathematical interpretation, and it does not mean that the model assumes any absorption effects by the gas.

Furthermore, we also define in advance the following integral kernel averaged over the initial direction of the

particle

$$\begin{aligned} K(\mathbf{r}, \boldsymbol{\Omega}, t | \mathbf{r}', t') &= \frac{1}{S_d} \oint_{S_d} d\Omega' K(\mathbf{r}, \boldsymbol{\Omega}, t | \mathbf{r}', \boldsymbol{\Omega}', t') \\ &= \frac{1}{S_d} e^{-n\sigma \|\mathbf{r}-\mathbf{r}'\|} \delta(\mathbf{r} - \mathbf{r}' - v\boldsymbol{\Omega}(t-t')), \end{aligned} \quad (119)$$

where S_d is the surface of the unit d -ball given in Eq. (1). This kernel describes an initially spherical wave packet, but still depends on the direction $\boldsymbol{\Omega}$. If we assume that the initial state is such a spherical state

$$f(\mathbf{r}, \boldsymbol{\Omega}, t_0) = \frac{1}{S_d} \delta(\mathbf{r} - \mathbf{r}_0), \quad (120)$$

then the Boltzmann equation (116) can be rewritten in integral form [42]

$$\begin{aligned} f(\mathbf{r}, \boldsymbol{\Omega}, t) &= K(\mathbf{r}, \boldsymbol{\Omega}, t | \mathbf{r}_0, t_0) \\ &+ \int_{t_0}^t dt' \int_{\mathbb{R}^d} d\mathbf{r}' \oint_{S_d} d\Omega' K(\mathbf{r}, \boldsymbol{\Omega}, t | \mathbf{r}', \boldsymbol{\Omega}', t') \\ &\times nv \oint_{S_d} d\Omega'' \frac{d\sigma}{d\Omega}(\boldsymbol{\Omega}' | \boldsymbol{\Omega}'') f(\mathbf{r}', \boldsymbol{\Omega}'', t'). \end{aligned} \quad (121)$$

In order to match the point scattering model of Sec. II A, we assume that the cross section is isotropic, i.e., $\frac{d\sigma}{d\Omega} = \frac{\sigma}{S_d}$. The integral over $\boldsymbol{\Omega}''$ in Eq. (121) thus becomes trivial and leads to the particle density

$$\rho(\mathbf{r}, t) = \oint_{S_d} f(\mathbf{r}, \boldsymbol{\Omega}, t) d\Omega. \quad (122)$$

In addition, the outer integral over $\boldsymbol{\Omega}'$ can be simplified using the direction-averaged kernel (119). We get

$$\begin{aligned} f(\mathbf{r}, \boldsymbol{\Omega}, t) &= K(\mathbf{r}, \boldsymbol{\Omega}, t | \mathbf{r}_0, t_0) \\ &+ \int_{t_0}^t dt' \int_{\mathbb{R}^d} d\mathbf{r}' K(\mathbf{r}, \boldsymbol{\Omega}, t | \mathbf{r}', t') n\sigma v \rho(\mathbf{r}', t'). \end{aligned} \quad (123)$$

At this point, we can elegantly eliminate the dependency on the direction of motion in Eq. (123) by integration over $\boldsymbol{\Omega}$ in both members. The new direction-independent kernel is in this regard

$$K(\mathbf{r}, t | \mathbf{r}', t') = \oint_{S_d} d\Omega K(\mathbf{r}, \boldsymbol{\Omega}, t | \mathbf{r}', t'). \quad (124)$$

The integral (124) can be evaluated from Eq. (119) with the following property of the Dirac delta

$$\oint_{S_d} d\Omega \delta^{(d)}(\mathbf{r} - v t \boldsymbol{\Omega}) = \frac{\delta(\|\mathbf{r}\| - vt)}{\|\mathbf{r}\|^{d-1}}. \quad (125)$$

The result is

$$K(\mathbf{r}, t | \mathbf{r}', t') = \frac{e^{-n\sigma \|\mathbf{r}-\mathbf{r}'\|}}{S_d \|\mathbf{r} - \mathbf{r}'\|^{d-1}} \delta(\|\mathbf{r} - \mathbf{r}'\| - v(t-t')), \quad (126)$$

and really represents a spherical shell expanding in every direction at constant speed v . The integral equation (123) becomes

$$\begin{aligned} \rho(\mathbf{r}, t) &= K(\mathbf{r}, t | \mathbf{r}_0, t_0) \\ &+ \int_{t_0}^t dt' \int_{\mathbb{R}^d} d\mathbf{r}' K(\mathbf{r}, t | \mathbf{r}', t') n\sigma v \rho(\mathbf{r}', t'), \end{aligned} \quad (127)$$

which no longer depends on the direction of motion. Note that the elimination of the direction dependence is fundamentally allowed by the assumption of isotropic cross section.

Finally, one notices that the transport equation (127) is stationary in the sense that the physical properties of the scattering medium do not depend on time. Consequently, it is useful to apply an integral transform, such as the Laplace transform, to Eq. (127):

$$\rho(\mathbf{r}, s) = v \int_0^\infty dt e^{-st} \rho(\mathbf{r}, t). \quad (128)$$

The factor of v in Eq. (128) is motivated by dimensional reasons. The Laplace transform also applies to the transport kernel, which becomes

$$\begin{aligned} K(\mathbf{r} | \mathbf{r}') &= v \int_0^\infty dt e^{-st} K(\mathbf{r}, t | \mathbf{r}', 0) \\ &= \frac{e^{-(\gamma+n\sigma)\|\mathbf{r}-\mathbf{r}'\|}}{S_d \|\mathbf{r} - \mathbf{r}'\|^{d-1}}, \end{aligned} \quad (129)$$

where we used the notation $\gamma = \frac{s}{v}$. Note that we retrieve in Eq. (129) the behavior of the transport kernel (113). The advantage of the Laplace transform is that the time convolution in Eq. (127) reduces to a simple product. The result is

$$\rho(\mathbf{r}, s) = K(\mathbf{r} | \mathbf{r}_0) + \int_{\mathbb{R}^d} d\mathbf{r}' K(\mathbf{r} | \mathbf{r}') n\sigma \rho(\mathbf{r}', s), \quad (130)$$

which exactly coincides with the integral transport equation (114). This confirms the equivalence between equations (114) and (115).

D. Uniform density matrix and coherence length

It is useful to derive the exact solution of the Bethe-Salpeter equation (109) in the special case of an infinite and homogeneous medium, to get a better idea of the local structure of the density matrix. We will also assume that the initial state of the particle, $\hat{\rho}_0$, is uniformly distributed in space

$$\hat{\rho}_0 = \rho_0 \int_{\mathbb{R}^d} d\mathbf{r}_0 |\mathbf{r}_0\rangle \langle \mathbf{r}_0| = \rho_0 \hat{1}. \quad (131)$$

The prefactor ρ_0 in Eq. (131) is arbitrary. We will fix it at the end of the calculation. Given these assumptions,

we consider the following ansatz for the average density matrix

$$\langle \hat{\rho}(s) \rangle = A \langle \hat{Q}(k) \rangle \langle \hat{Q}^\dagger(k) \rangle, \quad (132)$$

where A is a normalization factor that we will also fix at the end. Note that the product of effective propagators in Eq. (132) can be expanded using the first resolvent identity [35]

$$\begin{aligned} \langle \hat{Q} \rangle \langle \hat{Q}^\dagger \rangle &= -\frac{\langle \hat{Q}(k) \rangle - \langle \hat{Q}^\dagger(k) \rangle}{2i \operatorname{Im}(k^2 - nF)} \\ &= -\frac{1}{k_0(\gamma + n\sigma)} \operatorname{Im} \langle \hat{Q}(k) \rangle, \end{aligned} \quad (133)$$

where we have used $\gamma = 2k_i$ and $\operatorname{Im} F(k) \simeq -k_0\sigma(k_0)$ in the weak scattering regime. Inserting the ansatz (132) into the Bethe-Salpeter equation (109), we get

$$\begin{aligned} \langle \hat{Q} \rangle \langle \hat{Q}^\dagger \rangle &= \frac{\rho_0}{A} \langle \hat{Q} \rangle \langle \hat{Q}^\dagger \rangle + n |F(k)|^2 \\ &\times \int_{\mathbb{R}^d} \langle \hat{Q} \rangle |x\rangle \langle x| \langle \hat{Q} \rangle \langle \hat{Q}^\dagger \rangle |x\rangle \langle x| \langle \hat{Q}^\dagger \rangle dx. \end{aligned} \quad (134)$$

Since the medium is infinite, the effective propagator $\langle \hat{Q}(k) \rangle$ is given by Eq. (49) and the diagonal matrix element $\langle x| \langle \hat{Q} \rangle \langle \hat{Q}^\dagger \rangle |x\rangle$ does not depend on the position x . In addition, using Eq. (133), we find in the weak scattering regime

$$\langle x| \langle \hat{Q} \rangle \langle \hat{Q}^\dagger \rangle |x\rangle \simeq \frac{\pi\mu(k_0)}{k_0(\gamma + n\sigma)}. \quad (135)$$

Thus, using Eq. (135) and the resolution of identity $\hat{1} = \int_{\mathbb{R}^d} |x\rangle \langle x| dx$, the integral equation (134) reduces to

$$\begin{aligned} \langle \hat{Q} \rangle \langle \hat{Q}^\dagger \rangle &= \frac{\rho_0}{A} \langle \hat{Q} \rangle \langle \hat{Q}^\dagger \rangle \\ &+ n |F(k)|^2 \frac{\pi\mu(k_0)}{k_0(\gamma + n\sigma)} \langle \hat{Q} \rangle \langle \hat{Q}^\dagger \rangle. \end{aligned} \quad (136)$$

Finally, we use the point cross section formula (19) to obtain

$$\langle \hat{Q} \rangle \langle \hat{Q}^\dagger \rangle = \frac{\rho_0}{A} \langle \hat{Q} \rangle \langle \hat{Q}^\dagger \rangle + \frac{n\sigma}{\gamma + n\sigma} \langle \hat{Q} \rangle \langle \hat{Q}^\dagger \rangle, \quad (137)$$

which is indeed true if the normalization factor A satisfies

$$\frac{A}{\rho_0} = \frac{1}{1 - \frac{n\sigma}{\gamma + n\sigma}} = \frac{1}{\gamma}(\gamma + n\sigma). \quad (138)$$

Therefore, combining Eqs. (133) and (138) into the density matrix of Eq. (132), we can write

$$\langle \hat{\rho}(s) \rangle = -\frac{\rho_0}{k_0\gamma} \operatorname{Im} \langle \hat{Q}(k) \rangle. \quad (139)$$

The result (139) still depends on time through the variable $\gamma = s/v$ which appears in the denominator but also

in $k = k_0 + \frac{1}{2}\gamma$. Here, we are not interested in the possible transient of the density matrix, but only in its long time limit. This limit can be determined without taking the inverse Laplace transform in time thanks to the final value theorem

$$\hat{\rho}_\infty = \lim_{t \rightarrow \infty} \langle \hat{\rho}(t) \rangle = \lim_{s \rightarrow 0^+} s \langle \hat{\rho}(s) \rangle. \quad (140)$$

We quickly find from Eq. (139)

$$\hat{\rho}_\infty = -\frac{\rho_0 v}{k_0} \operatorname{Im} \langle \hat{Q}(k_0) \rangle. \quad (141)$$

In the following calculations, we will set the arbitrary normalization factor to $\rho_0 = k_0/v$ to get rid of the irrelevant prefactors in Eq. (141). Using Eq. (49) and the far-field behavior (14), one deduces that the imaginary part of the effective Green function is essentially the same as the free Green function but with an additional exponential decay factor [7]

$$\begin{aligned} -\operatorname{Im} \langle Q(k, \mathbf{r} | \mathbf{r}') \rangle &= -\operatorname{Im} G(\kappa, \mathbf{r} | \mathbf{r}') \\ &\simeq I(k_0, r) e^{-\operatorname{Im} \kappa r}, \end{aligned} \quad (142)$$

where $r = \|\mathbf{r} - \mathbf{r}'\|$ and $I(k, r) = -\operatorname{Im} G(k, r)$. The imaginary part of the effective wavenumber $\kappa(k)$ in Eq. (142) is equal to $\frac{n\sigma}{2}$ according to Eq. (52) and the fact that $k_i \rightarrow 0^+$ due to Eq. (140). Thus, the density matrix (141) reads in position space

$$\rho_\infty(\mathbf{r}, \mathbf{r}') = I(k_0, r) e^{-\frac{n\sigma}{2} r}. \quad (143)$$

This expression is even more explicit using the far-field behavior (14). Indeed, we have

$$\begin{aligned} \rho_\infty(\mathbf{r}, \mathbf{r}') &\xrightarrow{r \rightarrow \infty} \frac{1}{2k_0} \left(\frac{k_0}{2\pi r} \right)^{\frac{d-1}{2}} \\ &\times \sin \left(k_0 r - \frac{\pi(d-3)}{4} \right) e^{-\frac{n\sigma}{2} r}. \end{aligned} \quad (144)$$

It is worth noting that $I(k_0, r)$ in Eq. (143) corresponds to the free-space density matrix, because the same result would have been found from the uniform statistical mixture of momentum states

$$\hat{\rho} = \oint_{S_d} |k_0 \Omega\rangle \langle k_0 \Omega| d\Omega. \quad (145)$$

According to Eqs. (17) and (18) of Ref. [17], this would lead to the position-space matrix $\rho(\mathbf{r}, \mathbf{r}') \propto I(k_0, \|\mathbf{r} - \mathbf{r}'\|)$, which is close to Eq. (143). Alternatively, a statistical mixture in position space could have been constructed by integrating the free Green function $G(k_0, \mathbf{r} | \mathbf{r}_0)$ over the source point \mathbf{r}_0 . This would have

given us⁴

$$\begin{aligned} \rho(\mathbf{r}, \mathbf{r}') &\propto \int_{\mathbb{R}^d} G(k_0, \mathbf{r} \mid \mathbf{r}_0) G^*(k_0, \mathbf{r}' \mid \mathbf{r}_0) d\mathbf{r}_0 \\ &\propto I(k_0, \|\mathbf{r} - \mathbf{r}'\|), \end{aligned} \quad (146)$$

which is again very close to Eq. (143) but without the factor $e^{-\frac{n\sigma}{2}\|\mathbf{r}-\mathbf{r}'\|}$. This exponential factor comes from the loss of spatial coherence of the wave due to the average on the disorder. It means that the local description of the wave as a pure spherical wave, which remains valid at small scale, becomes less meaningful on lengths much larger than the mean free path $\ell_s = (n\sigma)^{-1}$. This is an important result, because it shows that two wave packets far enough to each other are statistically independent, and thus live different collision stories.

In practice, it is customary to measure the characteristic length beyond which the statistical correlations are lost using the standard deviation of the distribution $|\rho(\mathbf{r}, \mathbf{r}')|^2$ around a reference point. This quantity is known as the *coherence length* and is defined by [22, 23, 43, 44]

$$\Lambda(\mathbf{r}_0)^2 = \frac{\int_{\mathbb{R}^d} \|\mathbf{r} - \mathbf{r}_0\|^2 |\rho(\mathbf{r}, \mathbf{r}_0)|^2 d\mathbf{r}}{\int_{\mathbb{R}^d} |\rho(\mathbf{r}, \mathbf{r}_0)|^2 d\mathbf{r}}. \quad (147)$$

Note that this characteristic length depends on the reference point \mathbf{r}_0 . Since the density matrix is Hermitian ($\rho(\mathbf{r}, \mathbf{r}') = \rho^*(\mathbf{r}', \mathbf{r})$), the definition (147) is symmetric with respect to the exchange of variables $\mathbf{r} \leftrightarrow \mathbf{r}_0$. The coherence length can be explicitly obtained for the density matrix Eq. (143) using its far-field behavior (144). In the weak scattering regime (77), the fast oscillations of the sine function in Eq. (144) can be asymptotically approached by the average value $\sin^2 x = \frac{1}{2}$, and the integrals involved in Eq. (147) read

$$\begin{cases} \int_{\mathbb{R}^d} |\rho_\infty(\mathbf{r}, \mathbf{0})|^2 d\mathbf{r} & \xrightarrow{k_0 \gg n\sigma} \frac{\pi\mu(k_0)}{2k_0 n\sigma}, \\ \int_{\mathbb{R}^d} \|\mathbf{r}\|^2 |\rho_\infty(\mathbf{r}, \mathbf{0})|^2 d\mathbf{r} & \xrightarrow{k_0 \gg n\sigma} \frac{\pi\mu(k_0)}{k_0 (n\sigma)^3}. \end{cases} \quad (148)$$

In Eq. (148), we have set the arbitrary position to $\mathbf{r}_0 = \mathbf{0}$, because anyway the state (143) is invariant under spatial translations due to the uniform initial condition (131). Therefore, the sought coherence length is given by

$$\Lambda(\mathbf{r}_0)^2 = \frac{2}{(n\sigma)^2} = 2\ell_s^2. \quad (149)$$

This results shows, without surprise, that the coherence length equals the mean free path, up to a factor $\sqrt{2}$. In

this model, the mean free path is thus not only the mean distance between two successive collisions, but also the characteristic decay length of the autocorrelation function of the wave function, i.e., $\langle \rho(\mathbf{r}, \mathbf{r}') \rangle = \langle \psi(\mathbf{r}) \psi^*(\mathbf{r}') \rangle$. The two main consequences of the result (149) are as follows. First, it definitely confirms the interpretation of the exponential evanescence of the average Green function highlighted in Eq. (55) as being due to phase averaging [7, 45–47]. Second, this interpretation of the mean free path reinforces the analogy between the classical phase averaging in disordered media and the quantum decoherence in a gas [22, 23] already mentioned at the beginning of Sec. III C.

E. Diffusion approximation

In this section, we solve the integral equation (114) in the diffusion approximation for a spherical homogeneous medium of radius R . In this regard, we assume that the medium is much larger than the mean free path ($R \gg \ell_s$) or equivalently $n\sigma R \gg 1$. In the end of this section, we show that the diffusion approximation leads to an accurate estimate of the depth of the resonance band in Figs. 4(a) and 4(b), but also in Fig. 6 of Ref. [18], with respect to the real k axis for $d \geq 2$.

1. Diffusion equation

One way to the diffusion approximation consists in estimating the convolution integral in Eq. (114)

$$K * (n\sigma \langle \rho \rangle) = n\sigma \int_{\mathcal{V}} K(\mathbf{r} \mid \mathbf{r}') \langle \rho(\mathbf{r}') \rangle d\mathbf{r}', \quad (150)$$

where $\mathcal{V} = \mathcal{B}_d(R)$ denotes the spherical volume of the medium. We first look at the bulk of the medium, that is to say, far away from the boundary ($R - \|\mathbf{r}\| \gg \ell_s$). In this region, it is reasonable to extend the integral to \mathbb{R}^d , hence neglecting the possible edge effects. We will consider the special case of the boundary equation later. Omitting the constant prefactor $n\sigma$, the convolution integral (150) reads

$$K * \langle \rho \rangle = \int_{\mathbb{R}^d} K(\mathbf{r} \mid \mathbf{r}') \langle \rho(\mathbf{r}') \rangle d\mathbf{r}'. \quad (151)$$

On length scales much larger than the mean free path ($r \gg \ell_s$), an excellent approximation of the kernel $K(\mathbf{r} \mid \mathbf{r}')$ is

$$K(\mathbf{r} \mid \mathbf{r}') \simeq \frac{e^{-(\gamma+n\sigma)\|\mathbf{r}-\mathbf{r}'\|}}{S_d \|\mathbf{r} - \mathbf{r}'\|^{d-1}}, \quad (152)$$

according to Eq. (113). Since $n\sigma$ is very large, the kernel $K(\mathbf{r} \mid \mathbf{r}')$ looks like the Dirac delta function $\delta(\mathbf{r} - \mathbf{r}')$, but with a nonzero variance. To exploit this feature, we

⁴ Strictly speaking, this integral does not converge, hence the vague proportionality signs. In principle, it should be regularized using a finite integration volume or giving to the wavenumber a small positive imaginary part, but this is not shown here.

expand the density $\langle \rho(\mathbf{r}') \rangle$ in the neighborhood of the observation point \mathbf{r}

$$\begin{aligned} \langle \rho(\mathbf{r}') \rangle &= \langle \rho(\mathbf{r}) \rangle + (r'_i - r_i) \frac{\partial}{\partial r_i} \langle \rho(\mathbf{r}) \rangle \\ &+ \frac{1}{2!} (r'_i - r_i)(r'_j - r_j) \frac{\partial}{\partial r_i} \frac{\partial}{\partial r_j} \langle \rho(\mathbf{r}) \rangle + \dots, \end{aligned} \quad (153)$$

where we have assumed the implicit summation of repeated indices. We hope that the first three terms of Eq. (153) will suffice to approach $\langle \rho(\mathbf{r}') \rangle$. The convolution integral (151) then amounts to evaluating the first moments of the distribution $K(\mathbf{r} | \mathbf{r}')$. The zero-order moment reads

$$\int_{\mathbb{R}^d} \frac{e^{-(\gamma+n\sigma)\|\mathbf{r}-\mathbf{r}'\|}}{S_d \|\mathbf{r}-\mathbf{r}'\|^{d-1}} d\mathbf{r}' = \frac{1}{\gamma+n\sigma}. \quad (154)$$

This can be easily shown using the translational and rotational invariances of the integral and the fact that $d\mathbf{r}' = S_d (r')^{d-1} dr'$. The remaining integral is just $\int_0^\infty e^{-\beta x} dx = \frac{1}{\beta}$. The first-order moment

$$\int_{\mathbb{R}^d} \frac{e^{-(\gamma+n\sigma)\|\mathbf{r}-\mathbf{r}'\|}}{S_d \|\mathbf{r}-\mathbf{r}'\|^{d-1}} (\mathbf{r}' - \mathbf{r}) d\mathbf{r}' = \mathbf{0}, \quad (155)$$

is equal to the zero vector, because the distribution is symmetric with respect to the point $\mathbf{r}' = \mathbf{r}$. This also means that the particle does not undergo any drift or external forces. In fact, all the odd order moments are zero for the same reason. The second-order moment, which is a 3×3 matrix, reads

$$\int_{\mathbb{R}^d} \frac{e^{-(\gamma+n\sigma)\|\mathbf{r}-\mathbf{r}'\|}}{S_d \|\mathbf{r}-\mathbf{r}'\|^{d-1}} (r'_i - r_i)(r'_j - r_j) d\mathbf{r}' = \frac{2!}{(\gamma+n\sigma)^3} \frac{\delta_{ij}}{d}. \quad (156)$$

The off-diagonal elements ($i \neq j$) are zero because of the spherical symmetry of the distribution. In addition, the three diagonal elements ($i = j$) are equal for the same reason. These elements can be calculated in spherical coordinates, letting $r_i = r \cos \theta$, but we do not show it here explicitly. Combining Eqs. (154), (155) and (156), the convolution integral (151) is approached by

$$K * \langle \rho \rangle \simeq \frac{\langle \rho(\mathbf{r}) \rangle}{\gamma+n\sigma} + \frac{\nabla_{\mathbf{r}}^2 \langle \rho(\mathbf{r}) \rangle}{d(\gamma+n\sigma)^3}. \quad (157)$$

The integral transport equation (114) then becomes

$$\langle \rho(\mathbf{r}) \rangle = K(\mathbf{r} | \mathbf{r}_0) + n\sigma \left(\frac{\langle \rho(\mathbf{r}) \rangle}{\gamma+n\sigma} + \frac{\nabla_{\mathbf{r}}^2 \langle \rho(\mathbf{r}) \rangle}{d(\gamma+n\sigma)^3} \right), \quad (158)$$

which, after multiplying both sides by $(\gamma+n\sigma)$, reads

$$\gamma \langle \rho(\mathbf{r}) \rangle = (\gamma+n\sigma)K(\mathbf{r} | \mathbf{r}_0) + \frac{n\sigma}{d(\gamma+n\sigma)^2} \nabla_{\mathbf{r}}^2 \langle \rho(\mathbf{r}) \rangle. \quad (159)$$

Note that, according to the zero-order moment (154), the product $(\gamma+n\sigma)K(\mathbf{r} | \mathbf{r}_0)$ in Eq. (159) can be approached by a Dirac delta function. In addition, since we are only interested in time scales much longer than the intercollisional time ($t \gg (n\sigma v)^{-1}$), as we can see in Fig. 5, the Laplace variable γ is much smaller than $n\sigma$ and can be neglected in the rightmost term of Eq. (159). Therefore, we can write from Eq. (159)

$$\gamma \langle \rho(\mathbf{r}, \gamma) \rangle = \delta(\mathbf{r} - \mathbf{r}_0) + \frac{1}{dn\sigma} \nabla_{\mathbf{r}}^2 \langle \rho(\mathbf{r}, \gamma) \rangle. \quad (160)$$

To let appear the diffusion equation out of Eq. (160), we have to perform the inverse Laplace transform in time defined in Eq. (70)

$$\langle \rho(\mathbf{r}, t) \rangle = \frac{1}{2\pi i} \int_{-i\infty}^{i\infty} e^{\gamma v t} \langle \rho(\mathbf{r}, \gamma) \rangle d(\gamma v), \quad (161)$$

recalling that $s = \gamma v$. This is why, in Eq. (160), we have stressed the dependence of $\langle \rho(\mathbf{r}) \rangle$ on γ . We ultimately obtain the diffusion equation

$$\frac{\partial}{\partial t} \langle \rho(\mathbf{r}, t) \rangle - D \nabla_{\mathbf{r}}^2 \langle \rho(\mathbf{r}, t) \rangle = \delta(\mathbf{r} - \mathbf{r}_0) \delta(t), \quad (162)$$

where the parameter D is the *diffusivity*, or diffusion constant, characterizing the propagation of the particle in the medium. It reads

$$D = \frac{v}{dn\sigma} = \frac{v\ell_s}{d}. \quad (163)$$

Note that the right-hand side of Eq. (162) contains a source term at $\mathbf{r} = \mathbf{r}_0$ at time $t = 0$. This is consistent with the assumptions made in Sec. III A about the initial wave packet $\hat{\rho}_0 = |\mathbf{r}_0\rangle \langle \mathbf{r}_0|$. The diffusion equation (162) can be solved in an infinite medium. Setting $\mathbf{r}_0 = \mathbf{0}$, the result is [7]

$$\langle \rho(\mathbf{r}, t) \rangle = \frac{1}{(4\pi Dt)^{\frac{d}{2}}} \exp\left(-\frac{r^2}{4Dt}\right) \Theta(t), \quad (164)$$

where $\Theta(t)$ denotes the Heaviside step function given by Eq. (94). Expression (164) is a normalized Gaussian distribution. The variance of this distribution is given by

$$\langle \mathbf{r}(t)^2 \rangle = \int_{\mathbb{R}^d} \|\mathbf{r}\|^2 \langle \rho(\mathbf{r}, t) \rangle d\mathbf{r} = 2dDt = 2\ell_s vt, \quad (165)$$

and thus linearly increases in time. In contrast, the free-space propagation of a spherically symmetric wave packet, such as in Eq. (99), is characterized by a variance going as $\mathcal{O}(t^2)$. The slower behavior $\mathcal{O}(t)$ in Eq. (165) is due to the multiple collisions with the scatterers. This confirms that the propagation of the particle is not free.

2. Boundary condition

Aside from the equation in the bulk, in a finite medium, we also need a condition on the density at the boundary.

Since the medium is much larger than the mean free path, it can be approached by a semi-infinite region

$$\mathcal{V} \simeq \{\mathbf{r} \in \mathbb{R}^d \mid \mathbf{r} \cdot \mathbf{n} \leq 0\}, \quad (166)$$

where \mathbf{n} is the outward-pointing normal vector to the boundary of the medium. This assumption is motivated by the fact that, at the scale of the mean free path, the boundary is perceived as nearly flat. In this way, the boundary is just an infinite plane of equation $\mathbf{r} \cdot \mathbf{n} = 0$. In order to obtain a boundary condition on $\langle \rho(\mathbf{r}) \rangle$, we will approximate the integral transport equation (114) for any point \mathbf{r} on the boundary. More specifically, we want to estimate the integral

$$K * \langle \rho \rangle = \int_{\mathbf{r}' \cdot \mathbf{n} \leq 0} K(\mathbf{r} \mid \mathbf{r}') \langle \rho(\mathbf{r}') \rangle d\mathbf{r}', \quad (167)$$

where the integration domain covers the semi-infinite region (166). As done in Eq. (153), we expand the density $\langle \rho(\mathbf{r}') \rangle$ in Taylor series at $\mathbf{r}' = \mathbf{r}$

$$\langle \rho(\mathbf{r}') \rangle = \langle \rho(\mathbf{r}) \rangle + (\mathbf{r}' - \mathbf{r}) \cdot \nabla_{\mathbf{r}} \langle \rho(\mathbf{r}) \rangle + \dots \quad (168)$$

We neglect the higher order terms in Eq. (168), because we do not want the boundary condition to possess a second order derivative. Indeed, the diffusion equation (159) is of second order in space. Note that, in Eq. (167), the observation point \mathbf{r} is supposed to lie on the boundary, i.e., to satisfy $\mathbf{r} \cdot \mathbf{n} = 0$. Without loss of generality, we can set $\mathbf{r} = \mathbf{0}$ due to the translational symmetry of Eq. (167) in the plane of the boundary. The zero-order moment of the kernel reads

$$\begin{aligned} \int_{\mathbf{r}' \cdot \mathbf{n} \leq 0} K(\mathbf{0} \mid \mathbf{r}') d\mathbf{r}' &= \int_{\mathbf{r}' \cdot \mathbf{n} \leq 0} \frac{e^{-(\gamma+n\sigma)r'}}{S_d(r')^{d-1}} d\mathbf{r}' \\ &= \frac{1}{2(\gamma+n\sigma)}. \end{aligned} \quad (169)$$

This is just half the result (154) since it is integrated over half the space. The first-order moment

$$\int_{\mathbf{r}' \cdot \mathbf{n} \leq 0} \mathbf{r}' K(\mathbf{0} \mid \mathbf{r}') d\mathbf{r}' = \int_{\mathbf{r}' \cdot \mathbf{n} \leq 0} \mathbf{r}' \frac{e^{-(\gamma+n\sigma)r'}}{S_d(r')^{d-1}} d\mathbf{r}', \quad (170)$$

requires more caution because it is not spherically symmetric. Thus, we need to resort to spherical coordinates. Using the differential volume element in spherical coordinates

$$d\mathbf{r} = S_{d-1}(\sin \theta) d\theta r^{d-1} dr, \quad (171)$$

and projecting over the normal vector \mathbf{n} , Eq. (170) becomes

$$\begin{aligned} \int_{\mathbf{r}' \cdot \mathbf{n} \leq 0} (\mathbf{r}' \cdot \mathbf{n}) K(\mathbf{0} \mid \mathbf{r}') d\mathbf{r}' \\ = \frac{S_{d-1}}{S_d} \int_{\frac{\pi}{2}}^{\pi} d\theta \cos \theta (\sin \theta)^{d-2} \int_0^{\infty} dr' r' e^{-(\gamma+n\sigma)r'}. \end{aligned} \quad (172)$$

In Eq. (172), θ denotes the angle between \mathbf{r}' and the normal \mathbf{n} . The radial and angular integrals of Eq. (172) are elementary, leading to

$$\int_{\mathbf{r}' \cdot \mathbf{n} \leq 0} (\mathbf{r}' \cdot \mathbf{n}) K(\mathbf{0} \mid \mathbf{r}') d\mathbf{r}' = \frac{S_{d-1}}{S_d} \frac{-1}{d-1} \frac{1}{(\gamma+n\sigma)^2}. \quad (173)$$

Restoring the arbitrary direction of the normal \mathbf{r} and using the fact that $V_d = S_d/d$, we finally obtain from Eq. (173)

$$\int_{\mathbf{r}' \cdot \mathbf{n} \leq 0} \mathbf{r}' K(\mathbf{0} \mid \mathbf{r}') d\mathbf{r}' = -\mathbf{n} \frac{V_{d-1}}{S_d} \frac{1}{(\gamma+n\sigma)^2}. \quad (174)$$

Due to the rotational symmetry of the integral in the plane of the boundary, there is no component of the first-order moment (174) parallel to the boundary. In addition, note the minus sign in the right-hand side of Eq. (174) which is a direct consequence of the integration domain $\mathbf{r}' \cdot \mathbf{n} \leq 0$. Combining Eqs. (169) and (174), the convolution integral (167) can be approximated by

$$\begin{aligned} \int_{\mathbf{r}' \cdot \mathbf{n} \leq 0} K(\mathbf{r} \mid \mathbf{r}') \langle \rho(\mathbf{r}') \rangle d\mathbf{r}' \\ \simeq \frac{\langle \rho(\mathbf{r}) \rangle}{2(\gamma+n\sigma)} - \frac{V_{d-1}}{S_d} \frac{\mathbf{n} \cdot \nabla_{\mathbf{r}} \langle \rho(\mathbf{r}) \rangle}{(\gamma+n\sigma)^2}. \end{aligned} \quad (175)$$

Now, we can substitute the approximation (175) into the integral equation (114). The source term $K(\mathbf{r} \mid \mathbf{r}_0)$ can be neglected, because we assume that it is located far away from the boundary, typically somewhere in the bulk. This gives us

$$\langle \rho(\mathbf{r}) \rangle = n\sigma \left(\frac{\langle \rho(\mathbf{r}) \rangle}{2(\gamma+n\sigma)} - \frac{V_{d-1}}{S_d} \frac{\mathbf{n} \cdot \nabla_{\mathbf{r}} \langle \rho(\mathbf{r}) \rangle}{(\gamma+n\sigma)^2} \right). \quad (176)$$

After some rearrangements, Eq. (176) becomes

$$\left(\gamma + \frac{n\sigma}{2} \right) \langle \rho(\mathbf{r}) \rangle + \frac{V_{d-1}}{S_d} \frac{n\sigma}{\gamma+n\sigma} \mathbf{n} \cdot \nabla_{\mathbf{r}} \langle \rho(\mathbf{r}) \rangle = 0. \quad (177)$$

When considering times much longer than the intercollisional time, γ can be neglected in front of $n\sigma$. Thus, we obtain from Eq. (177)

$$\frac{n\sigma}{2} \langle \rho(\mathbf{r}) \rangle + \frac{V_{d-1}}{S_d} \mathbf{n} \cdot \nabla_{\mathbf{r}} \langle \rho(\mathbf{r}) \rangle = 0. \quad (178)$$

This is a Robin boundary condition on the density $\langle \rho(\mathbf{r}) \rangle$ for all $\mathbf{r} \in \partial\mathcal{V}$. Since the coefficients of the two terms in Eq. (178) are positive, this condition expresses the fact that the density has an inward-facing gradient. In the limit $n\sigma \rightarrow \infty$, this condition reduces to a simple Dirichlet boundary condition: $\langle \rho(\mathbf{r}) \rangle = 0$. Although this regime is valid for a very large medium, we do not consider this extreme case for the moment.

F. Spatial profile of the wave function

In this section, we consider some implications of the diffusion equation on the square modulus of the wave function and we compare its predictions to the results of numerical simulations.

1. Quantum scars and configurational averaging

An example of square modulus of wave function for a single random configuration of $N = 10^3$ scatterers is shown in Fig. 9(a). See also the large simulation of Fig. 10(a) obtained for $N = 10^4$ scatterers. In both figures, the wave function is computed from the system (24), using the incident wave

$$\phi(\mathbf{r}) = G^+(k, \mathbf{r} | \mathbf{r}_0). \quad (179)$$

In addition, the particle is assumed to be created at the center of the medium ($\mathbf{r}_0 = \mathbf{0}$). The density in Fig. 9(a) strongly fluctuates at the scale of the wavelength. In particular, the scale of the angular fluctuations of $|\psi(\mathbf{r})|^2$ out of the medium ($\|\mathbf{r}\| \gg R$) is predicted by partial-wave theory to be

$$\Delta\theta = \frac{\pi}{kR}, \quad (180)$$

as given in Eq. (137) of Ref. [17]. In the case of Fig. 9(a), this gives fluctuation scale of one degree ($\Delta\theta \simeq 1^\circ$). In Fig. 10(a), one finds $\Delta\theta \simeq 0.3^\circ$.

In addition, one can see network-like structures at the scale of the mean free path ℓ_s in Figs. 9(a) and 10(a). The apparent filaments that compose them are reminiscent of *quantum scars*, which are considered in the literature [48, 49]. A quantum scar is an enhancement of the magnitude of the wave function around classically periodic orbits which are typically unstable. Strictly speaking, there is no such orbit in this model, since the cross section of points is classically equal to zero. However, in the quantum case, such collisions are enabled by the wave nature of the incident particle, because, as we have seen in Eq. (21), the point cross section is at most of the order of λ^{d-1} . The cross section is thus arbitrarily small but not zero in the semiclassical limit $\lambda \xrightarrow{\neq} 0$. Therefore, if we admit the existence of point collisions, then any closed path joining some of the scatterers may be considered as an unstable periodic orbit. It should be noted that the random point field contains⁵

$$C_{cy,p} = \begin{cases} \frac{N!}{2p(N-p)!} & \text{if } p \geq 3, \\ \frac{1}{2}N(N-1) & \text{if } p = 2, \end{cases} \quad (181)$$

orbits involving p points. The total number of orbits thus reads

$$C_{cy} = \sum_{p=2}^N C_{cy,p} \xrightarrow{N \rightarrow \infty} \frac{(N-1)!}{2} e^1. \quad (182)$$

⁵ There are $\binom{N}{p} = \frac{N!}{p!(N-p)!}$ ways to pick up p points out of N . This count is then multiplied by the number $\frac{1}{2}(p-1)!$ of closed cycles in a complete graph of p vertices.

The number (182) is so large in the limit $N \rightarrow \infty$, that we may expect quantum scarring to occur in many places. If this is confirmed, it is probably the first time quantum scars are observed for such a large disordered system.

On much larger scales than the mean free path, the density globally decreases between the center and the edge of the medium. This global behavior is well reproduced by the average density shown in Fig. 9(b). This suggests that the aspect of the wave density in an infinite disordered medium will be closer to Fig. 9(b) than to Fig. 9(a), because the medium will ultimately look uniform at such scale. This would support the validity of the configurational averaging made in the beginning of Sec. III B for a sufficiently large medium ($R \gg \ell_s$).

2. Stationary diffusion

Furthermore, we want to compare the prediction of the diffusion equation (160) to the numerical value of $\langle |\psi(\mathbf{r})|^2 \rangle$ in the ball-shaped point field. For this purpose, we assume that the wave packet is created at the center of the spherical medium ($\mathbf{r}_0 = \mathbf{0}$). In the stationary regime ($\gamma \rightarrow 0$), the Laplace-transformed diffusion equation (160) reads

$$\nabla_{\mathbf{r}}^2 \rho_{da}(\mathbf{r}) = -A \delta(\mathbf{r}), \quad (183)$$

where the subscript stands for *diffusion approximation*, and the amplitude factor is $A = dn\sigma$. However, the normalization convention in our numerical simulations is slightly different from what Eq. (160) prescribes. In these simulations, we assume that the source term in Eq. (114) is $|\langle Q(k, \mathbf{r} | \mathbf{r}_0) \rangle|^2$ and not $K(\mathbf{r} | \mathbf{r}_0)$. The correction is simply given by the prefactor in Eq. (112). Thus, we should have

$$A = dn\sigma \frac{\pi\mu(k_0)}{k_0}. \quad (184)$$

The general solution of the Poisson equation (183) reads

$$\rho_{da}(r) = \begin{cases} -\frac{A}{S_d} \frac{r^{2-d} - R_{\text{eff}}^{2-d}}{2-d} & \text{for } d \neq 2, \\ -\frac{A}{2\pi} \ln\left(\frac{r}{R_{\text{eff}}}\right) & \text{for } d = 2, \end{cases} \quad (185)$$

where the arbitrary parameter R_{eff} denotes the effective radius at which the density is supposed to vanish as if the medium was extended beyond R . Since the density must be positive everywhere, the effective radius is necessarily larger or equal to the actual radius R of the medium ($R_{\text{eff}} \geq R$). The effective radius has to be adjusted to satisfy the boundary condition (178), which can also be rewritten as

$$\frac{\rho_{da}(R)}{\partial_r \rho_{da}(R)} = -\frac{2V_{d-1}}{S_d} \ell_s. \quad (186)$$

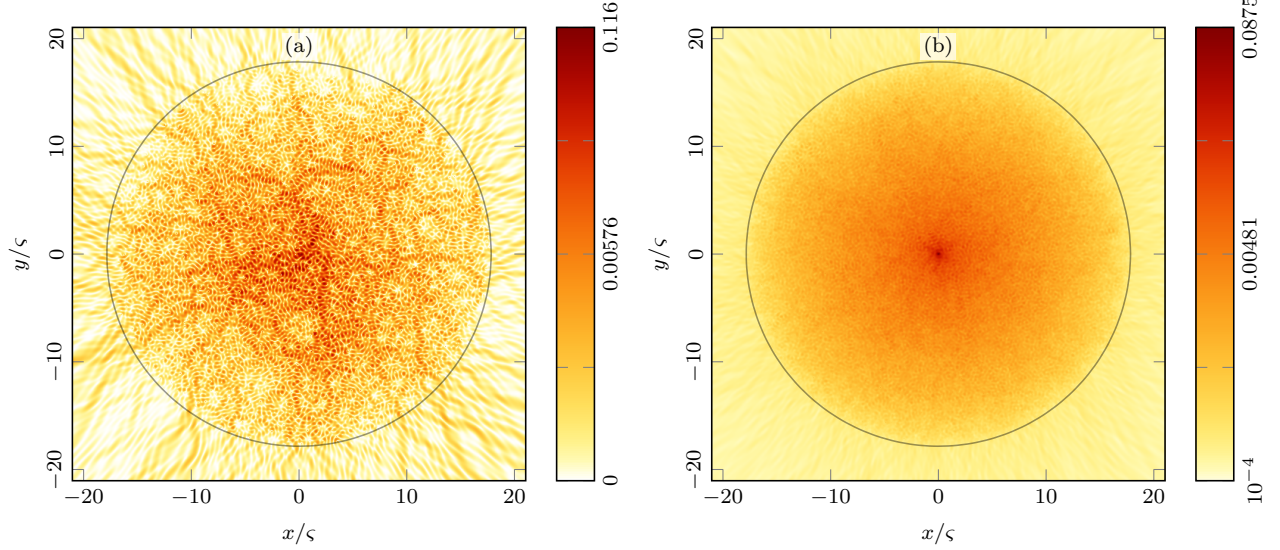


FIG. 9. (a) Square modulus of the wave function computed with MSModel [19] in a 2D disk-shaped random point field of $N = 10^3$ scatterers with $k = 10 \zeta^{-1}$. The scattering model is Eq. (20) and the mean free path is $\ell_s = 2.5 \zeta$. The point source is located at the center ($\mathbf{r}_0 = \mathbf{0}$). The circle depicts the medium boundary. (b) Same as panel (a) but averaged over 2^6 random configurations.

In order to satisfy Eq. (186), the effective radius R_{eff} in Eq. (185) must read

$$R_{\text{eff}} = \begin{cases} R \left(1 + (2-d) \frac{2V_{d-1} \ell_s}{S_d R} \right)^{\frac{1}{2-d}} & \text{for } d \neq 2, \\ R \exp \left(\frac{2V_{d-1} \ell_s}{S_d R} \right) & \text{for } d = 2, \end{cases} \quad (187)$$

Note that, if the mean free path is small enough ($\ell_s \ll R$), the expressions (187) can be effectively expanded at first order. We find

$$R_{\text{eff}} \simeq R + \frac{2V_{d-1}}{S_d} \ell_s. \quad (188)$$

Since the dimensionless factor $2V_{d-1}/S_d$ is of the order of one, the result (188) means that the effective radius is about the actual radius plus the mean free path. This is a known result of transport theory, which is, for instance, encountered in the neutronics of nuclear reactors [42].

The square modulus of the wave function numerically computed with MSModel [19] in a ball-shaped random point field for $N = 10^3$ is shown in Fig. 11. This figure actually represents the same situation as in Fig. 9, but in a cross-sectional view along the x axis. The similar cross-sectional view of Fig. 10(a) is shown in Fig. 12. In both Figs. 11 and 12, the dashed curve is the theoretical average density (185) predicted by the diffusion approximation. The matching with the numerical average for $r \leq R$ in Fig. 11(b) is remarkable, despite the apparent roughness of the diffusion approximation. Indeed, the scale parameter $R/\ell_s \simeq 7$ is not so large compared to one. Figures 11(a) and 12 seem to confirm that the

wave function in a single configuration globally follows the theoretical decrease of $\rho_{\text{da}}(r)$.

In the neighborhood of the source point at $\mathbf{r}_0 = \mathbf{0}$, the numerical average does not match the diffusion approximation in Fig. 11(b). The reason is that the diffusion approximation is not supposed to be accurate on scales shorter than the mean free path. Indeed, the amplitude of the singularity predicted by the diffusion approximation is not consistent with that of the Bethe-Salpeter equation (114). According to Eq. (110), the intensity near the source point \mathbf{r}_0 is approximately given by the effective Green function $|\langle Q(k, \mathbf{r} | \mathbf{r}_0) \rangle|^2$. This is confirmed by the matching between the solid and the dotted curves near $r = 0$ in Fig. 11(b).

Besides that, one notices a mismatch at the edge of the medium for $r \geq R$. This is due to the fact that the density (185) is only valid within the point field. In the outer region ($r \geq R$), the density behaves as the power law

$$\rho(r) \propto \frac{1}{r^{d-1}}. \quad (189)$$

This is given by the far-field behavior of Eq. (114) for $r \gg R$.

G. Depth of the resonance band

The integral equation (114) also provides a prediction of the position of the band of complex resonances seen in Fig. 6 of Ref. [18] but also in Figs. 4(a) and 4(b). The resonant states can be obtained as the eigenvectors of the Schrödinger equation without any source term, just like

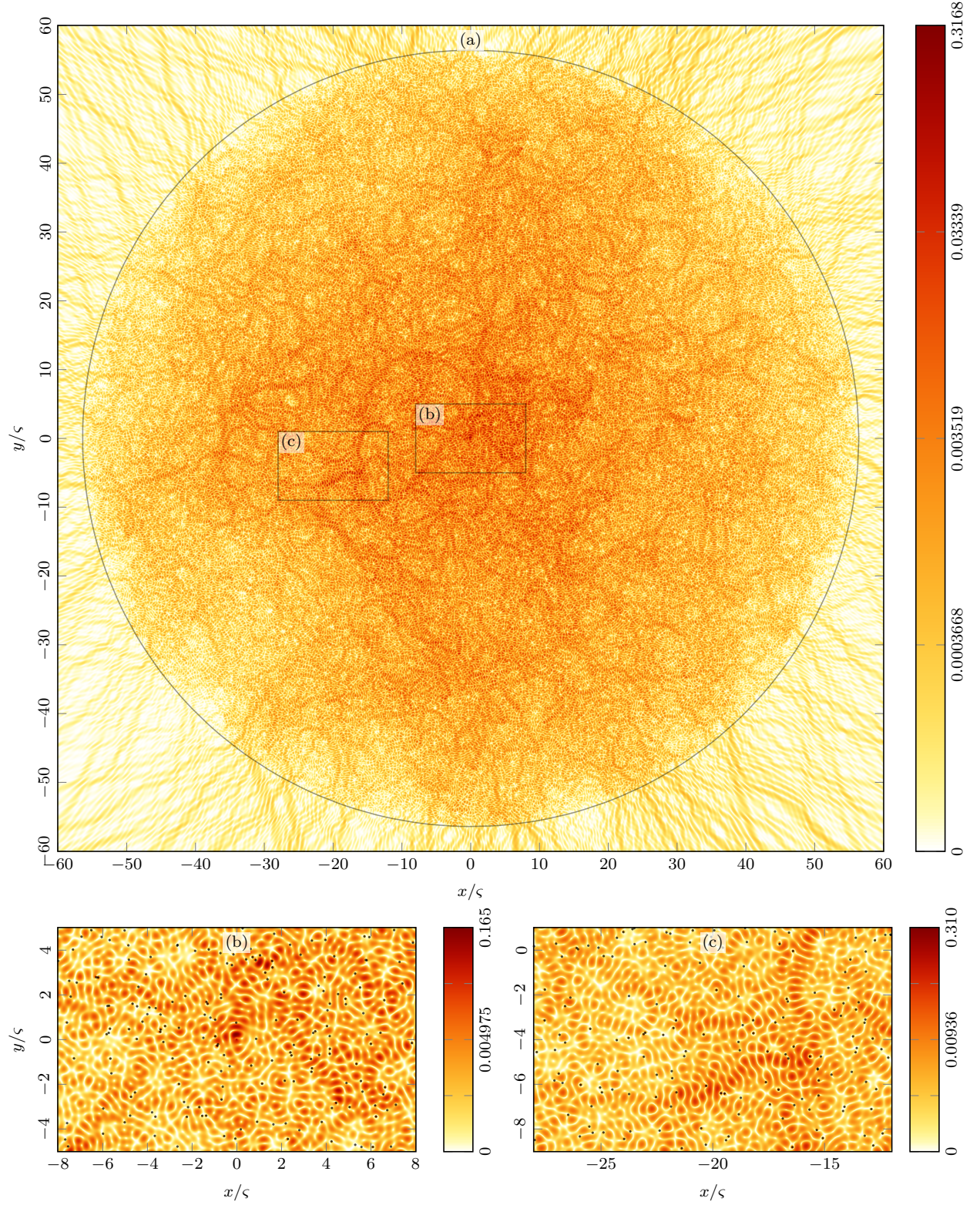


FIG. 10. Square modulus of the wave function computed with MSModel [19] in a 2D disk-shaped random point field for a single configuration of $N = 10^4$ scatterers with $k = 10\varsigma^{-1}$. The point source is at the center ($\mathbf{r}_0 = \mathbf{0}$) and the mean free path is $\ell_s = 2.5\varsigma$. The circle depicts the medium boundary. (a) 4-megapixel overview. Total computation time is about 80 minutes on an Intel Core i7 processor with four threads. (b) Enlargement of the central source point. The scatterers are depicted by small black dots. (c) Enlargement of a presumed quantum scar.

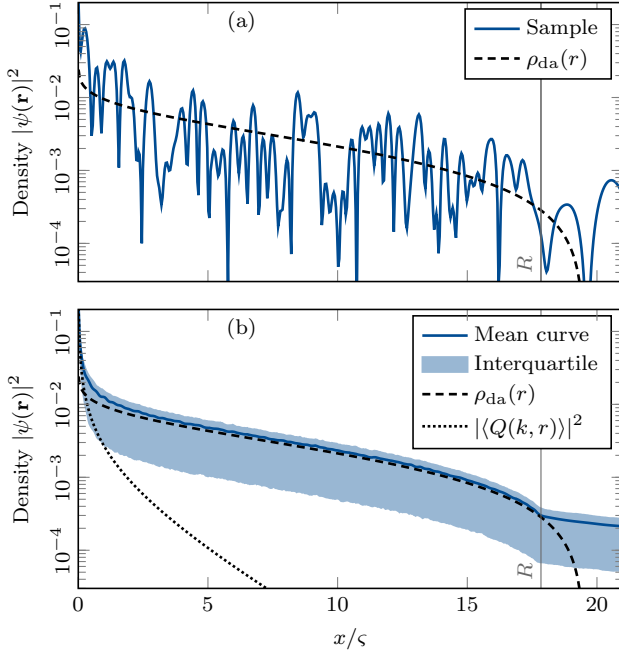


FIG. 11. (a) Cross-sectional view of Fig. 9(a) along the positive x semiaxis. The vertical gray line indicates the radius of the medium. The dashed curve is the diffusion approximation (185) using Eqs. (184) and (187). (b) Cross-sectional view of Fig. 9(b) averaged over 2^{14} configurations. The filled region is the numerically computed interquartile range of $|\psi(\mathbf{r})|^2$. The dotted curve is the square modulus of the effective Green function (49).

eigenstates but at complex energies. In the same way, in order to study the resonance band from Eq. (114), we need to set the source term $K(\mathbf{r} | \mathbf{r}_0)$ to zero and interpret the resulting equation

$$\langle \rho(\mathbf{r}) \rangle = \int_{\mathbb{R}^d} \frac{e^{-(\gamma+n\sigma)\|\mathbf{r}-\mathbf{r}'\|}}{S_d \|\mathbf{r}-\mathbf{r}'\|^{d-1}} n(\mathbf{r}') \sigma(k) \langle \rho(\mathbf{r}') \rangle d\mathbf{r}', \quad (190)$$

as an eigenvalue problem, where the free variable γ plays the role of the sought eigenvalue and the density $\langle \rho(\mathbf{r}) \rangle$ is the associated eigenfunction. The eigensystem (190) is more easily solved in the diffusion approximation. Using Eqs. (160) and (178), the integral equation (190) can be cast into

$$\begin{cases} \frac{\ell_s}{d} \nabla_{\mathbf{r}}^2 \langle \rho(\mathbf{r}) \rangle - \gamma \langle \rho(\mathbf{r}) \rangle = 0 & \text{for } r \leq R, \\ \frac{2V_{d-1}}{S_d} \ell_s \mathbf{n} \cdot \nabla_{\mathbf{r}} \langle \rho(\mathbf{r}) \rangle + \langle \rho(\mathbf{r}) \rangle = 0 & \text{for } r = R. \end{cases} \quad (191)$$

The first line of Eq. (191) is the Laplace-transformed diffusion equation, and the second line is the boundary condition at $r = R$. Indeed, we assume that the medium is spherical. The first line of Eq. (191) can be written in the more familiar form

$$(\nabla_{\mathbf{r}}^2 + \beta^2) \langle \rho(\mathbf{r}) \rangle = 0, \quad (192)$$

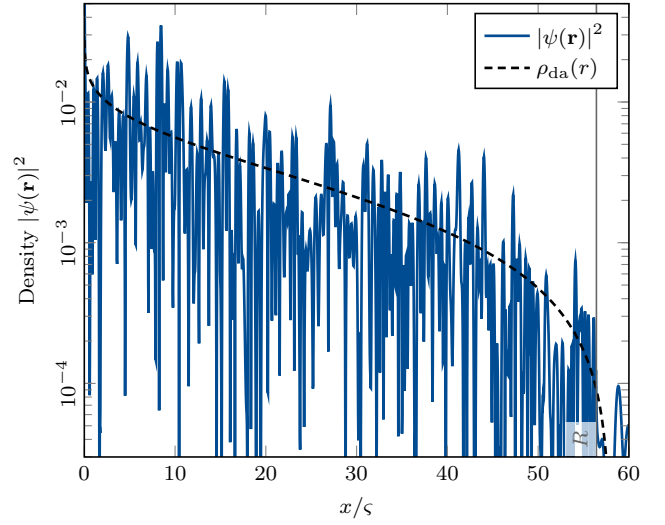


FIG. 12. Cross-sectional view of Fig. 10(a) along the positive x semiaxis. The vertical gray line indicates the radius of the medium. The dashed curve is the diffusion approximation (185) using Eqs. (184) and (187).

where β is the Fourier variable for space, analogous to a wavenumber. The solution of Eq. (192) reads

$$\langle \rho(r) \rangle = j_0^{(d)}(\beta r), \quad (193)$$

where $j_\ell^{(d)}(z)$ is the generalized spherical Bessel function defined in Eq. (62). It mainly depends on the Bessel function $J_{\frac{d-2}{2}}(z)$. Using Eq. (193), the differential problem (191) becomes the following nonlinear system for the pair (γ, β)

$$\begin{cases} \frac{\ell_s}{d} \beta^2 + \gamma = 0, \\ \frac{2V_{d-1}}{S_d} \beta \ell_s j_0^{(d)'}(\beta R) + j_0^{(d)}(\beta R) = 0. \end{cases} \quad (194)$$

The system of equations (194) is graphically solved in Fig. 13(a). The first equation corresponds to the parabola, and the second equation to the horizontal straight lines. The intersections between both are the eigenmodes of Eq. (191). The corresponding eigenvalues, denoted as β_n and γ_n , fully characterize the eigenmodes in space and time, respectively. The profiles of the first diffusion eigenmodes in space are shown in Fig. 13(b) based on Eq. (193).

Furthermore, the spectral decomposition of the diffusion problem (191) allows us to write the general solution for the density and its time evolution. Through inverse Laplace transform, one has the expansion

$$\langle \rho(\mathbf{r}, t) \rangle = \sum_{n=1}^{\infty} c_n e^{\gamma_n t} j_0^{(d)}(\beta_n r), \quad (195)$$

where v is the group velocity and c_n are arbitrary constants depending on the initial condition at $t = 0$. Since

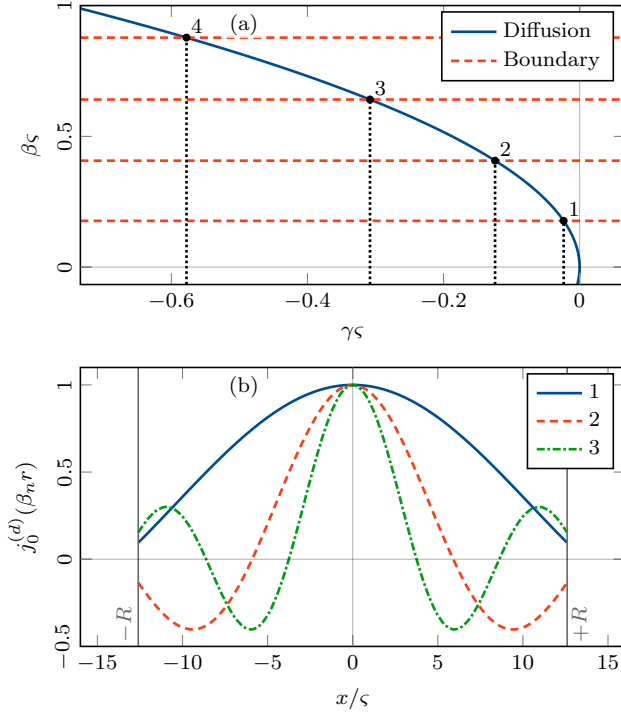


FIG. 13. (a) Graphical solution of the diffusion eigenmodes from Eq. (194) in the dual space (γ, β) for a 2D disk-shaped random point field with $N = 500$ scatterers. The parameters are $R = 12.6\zeta$ and $\ell_s = 1.5\zeta$. The black dots are the first four solutions: $n \in \{1, 2, 3, 4\}$. (b) First diffusion eigenmodes $n \in \{1, 2, 3\}$ in the position space from Eq. (193).

the density must be positive, the constant c_1 , associated with the fundamental mode, should be the largest one. Note that the values of γ_n are negative. Therefore, Eq. (195) describes the decay of the density in time due to the escape of the particle from the medium. In the long time limit ($t \rightarrow \infty$), the fundamental mode dominates the other ones, since γ_1 has the smallest value. Of course, the superiority of the fundamental mode is required by the constraint on the positivity of the density.

Although the boundary condition in Eq. (194) cannot be solved for β in closed form, it is possible to continue the calculation further if the mean free path is sufficiently small ($\ell_s \ll R$). Indeed, for a small enough ℓ_s , one may recognize the first order expansion of

$$j_0^{(d)}\left(\beta R + \frac{2V_{d-1}}{S_d}\beta\ell_s\right) = 0, \quad (196)$$

in the second equation of Eq. (194). Using the approximate effective radius (188), Eq. (196) can be simplified to

$$j_0^{(d)}(\beta R_{\text{eff}}) = 0. \quad (197)$$

Condition (197) obviously expresses the geometrical interpretation of R_{eff} as the point where the extrapolated density vanishes. This interpretation was already discussed near Eq. (185). The roots of Eq. (197) are given

by the zeros of $j_0^{(d)}(z)$, or, more explicitly, by the zeros of $J_{\frac{d-2}{2}}(z)$. Thus, we obtain the full spectrum of diffusion eigenmodes

$$\beta_n = \frac{j_{\frac{d-2}{2},n}}{R_{\text{eff}}}, \quad (198)$$

where $j_{\nu,n} \forall n \in \{1, 2, 3, \dots\}$ denotes the n -th zero of the Bessel function $J_\nu(z)$. The first zeros of interest are given in Tab. II for the lowest dimensions. According to

d	1	2	3	4
$n = 1$	$\frac{\pi}{2}$	2.40483...	π	3.83171...
$n = 2$	$\frac{3\pi}{2}$	5.52008...	2π	7.01559...
$n = 3$	$\frac{5\pi}{2}$	8.65373...	3π	10.1735...
$n = 4$	$\frac{7\pi}{2}$	11.7915...	4π	13.3237...
$n = 5$	$\frac{9\pi}{2}$	14.9309...	5π	16.4706...

TABLE II. First zeros of the Bessel function $J_{\frac{d-2}{2}}(z)$, denoted as $j_{\frac{d-2}{2},n}$ in the text [24]. No closed form exists for these zeros, except for $d = 1$ and $d = 3$.

the first line of Eq. (194), the values of γ associated to Eq. (198) read

$$\gamma_n = -\frac{\ell_s}{d} \left(\frac{j_{\frac{d-2}{2},n}}{R_{\text{eff}}} \right)^2. \quad (199)$$

The result (199) turns out to be an accurate approximation of the sought eigenvalue of Eq. (190). The quantity (199) is also related to the escape rate of the particle from the medium by $\Gamma_n = |\gamma_n| v$.

Finally, using the relationship $\gamma = 2k_i$ introduced in Eq. (54), the diffusion rate of Eq. (199) translates into the following estimate

$$k_{\text{diff},n} = -\frac{\ell_s}{2d} \left(\frac{j_{\frac{d-2}{2},n}}{R_{\text{eff}}} \right)^2, \quad (200)$$

for the position of the resonance band. The result (200) is considerably more accurate than Eq. (68) of Ref. [18] since it accounts for the Robin boundary condition (194) which is more precise than the Dirichlet condition $j_\ell^{(d)}(\beta R) = 0$ limited to infinitesimally small mean free path ($\ell_s \ll R$). It is also more general than Eq. (68) because it predicts other eigenmodes than the fundamental one.

The comparison between the prediction (200) and the numerical results is shown in Fig. 14 for the 2D and 3D cases. The resonance band in Fig. 14 is computed with MSModel [19] exploiting the resonance potential method of Ref. [18]. Note that the final increase of the density in Fig. 14(a) near $k_i = 1\zeta^{-1}$ is due to numerical round-off errors in computing the determinant of $M(k)$ and is thus not physical. This phenomenon was previously discussed near Eq. (66) of Ref. [18].

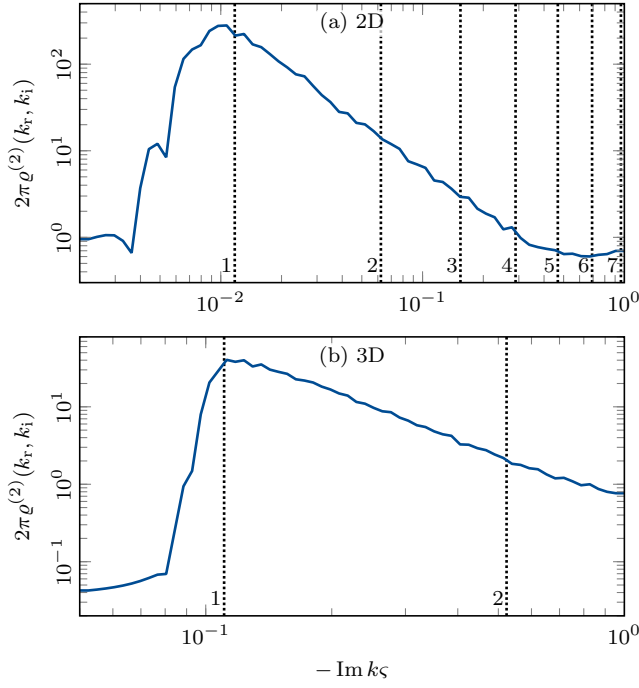


FIG. 14. (a) Cross-sectional view of the resonance density for a 2D disk-shaped random point field with $N = 500$ along the vertical axis $k_r = 6\zeta^{-1}$ and averaged over 2^{10} configurations. The parameters are $R = 12.6\zeta$ and $\ell_s = 1.5\zeta$. The vertical dotted lines indicate the diffusion eigenmodes given by Eq. (194). (b) Same as panel (a) but in the 3D case with $R = 4.92\zeta$ and $\ell_s = 2.865\zeta$.

The adequacy between the fundamental mode ($n = 1$) and the maximum of the resonance band in Fig. 14 is remarkable. This is especially true in 3D, because the scale parameter $n\sigma R = 1.72$ is not so much larger than one compared to what the diffusion approximation discussed in Sec. III E could have required. In fact, the quality of the approximation (200) greatly depends on the expression of R_{eff} and on the boundary condition. Indeed, if the magnitudes of R and ℓ_s are the same, there is a factor of two between R and R_{eff} , and thus a factor of four in $k_{\text{diff},n}$, which is significant.

Strangely, the other diffusion eigenmodes do not lead to any perceptible structure. We could have thought that Eq. (200) predicts the existence of additional bands deeper in the complex plane. However, we could not find any match, not even in much larger point fields, up to $N = 5000$. Only the fundamental mode seems to work. Furthermore, regarding the 1D case, these higher order modes do not coincide with the faint bands in Fig. 6(a) of Ref. [18]. All these observations would lead us to conjecture that these higher order diffusion eigenmodes do not exist in the quantum case. This discrepancy does not seem to be known in the quantum diffusion literature [7, 8].

IV. CONCLUSIONS

In this work, the distribution of the resonance poles of the Green function associated to the wave propagation in a random point field has been studied theoretically. This two-dimensional distribution in the complex plane of the wavenumber k was brought to light in Ref. [18] and presented two kinds of structure: peaks at small values of k and a band almost parallel to the real axis at larger values of k .

We showed in Sec. II that the location of peaks can be predicted by an effective Schrödinger equation for the average of the wave function over the configurations of the random point field. The complex resonances of this effective equation reproduce the ordered structure of peaks as seen in Fig. 4. These resonances are in fact very close to those obtained for the scattering on a transparent sphere. This means that, at small k , the wave only probes the spherical shape of the random point field without resolving the details due to the disorder. The critical wavelength separating the small- k from the large- k regimes is about twice the mean interscatterer distance.

Then, in Sec. III, we derived an integral transport equation known as the Bethe-Salpeter equation in order to describe the resonance band at large k . This derivation followed the diagrammatic approach in the ladder approximation which is valid in the weak scattering regime ($k\ell_s \gg 1$) [7, 8, 16]. The stationary intensity profile of the wave in the bulk predicted by the Bethe-Salpeter equation was successfully confirmed by the numerical simulations carried out with MSModel [19]. This verification was performed in particular for a large 2D random point field of $N = 10^4$ scatterers, as seen in Fig. 10. This simulation also revealed the existence of filaments in the square modulus of the wave function which we interpreted as quantum scars [48, 49]. The detailed study of these structures, including their possible links with the multiple-scattering resonances, is deferred to future works.

In Sec. III C, it was proved that the Bethe-Salpeter equation is equivalent to the linear Boltzmann equation, the central equation of classical transport theory. While supporting the physical meaning of the Bethe-Salpeter equation, this proof highlights the validity of this equation at any time up to a Laplace transform in time. This connection to time evolution is crucial to understand the relationship with the resonance distribution. Indeed, the resonant states evolve in time in contrast to the eigenstates of the Hamiltonian. Accordingly, it was suspected that the position of the resonance band is governed by the escape time of the particle from the medium. Guided by this idea, we searched for the eigenvalues and eigenvectors of the Bethe-Salpeter equation in the absence of a source term. This calculation was achieved in Sec. III G under the diffusion approximation, i.e., when the mean free path is much smaller than the radius of the point field ($\ell_s \ll R$). Accurate boundary conditions were used to take into account the relative smallness of the point

fields reachable by the simulations ($N < 10^3$) compared to the length of the mean free path. Several diffusion eigenmodes were found, but only the fundamental, which corresponds to the largest escape time, actually matched the maximum of the resonance band. However, the other modes did not cause an increase in the resonance density, as seen in Fig. 14. This led us to conjecture that the higher-order diffusion eigenmodes do not exist in the quantum case.

The issue of the absence of higher-order diffusion eigenmodes could be further investigated using other approaches such as the nonlinear sigma model [50]. This field-theoretical method is based on the average of some generating function over the realizations of a Gaussian random potential. Upon averaging, the linear wave equation in the disordered medium is then cast into a disorder-free nonlinear wave equation which can be solved semi-classically. This method has proven particularly effective in determining the full statistics of certain observables [50–52]. In the future, we plan to study the wave propagation in a random point field from the perspective of the nonlinear sigma model in order to characterize the resonance distributions of Figs. 4 and 14 more precisely.

ACKNOWLEDGMENTS

The present results were obtained during D.G.’s doctoral thesis defended in June 2022. The authors are grateful to Prof. Pierre Gaspard for useful discussions and for reviewing this manuscript. This work was supported by the Belgian National Fund for Scientific Research (F.R.S.-FNRS) as part of the “Research Fellow” (ASP - Aspirant) fellowship program. This work was also supported by the F.R.S.-FNRS as part of the Institut Interuniversitaire des Sciences Nucléaires (IISN) under Grant No. 4.45.10.08. It also received funding from the French National Research Agency (ANR) as part of the “MARS LIGHT” project.

Appendix A: Zeros of the Hankel function

In this appendix, we study the complex zeros of the Hankel function $H_\nu^+(z)$. In particular, we want to accurately estimate the location of these zeros in order to feed the numerical root-finding method considered in Sec. II C for Eq. (65). These complex zeros occur when looking for the deep resonance poles of the hard-sphere scattering. These resonance poles are very far from the real k axis and thus mostly formal, but we will need them later.

As a reminder, the hard-sphere scattering model is defined by the singular potential [53–56]

$$U(\mathbf{r}) = \begin{cases} +\infty & \text{for } \|\mathbf{r}\| \leq R, \\ 0 & \text{otherwise,} \end{cases} \quad (\text{A1})$$

in the wave equation (2). According to partial wave theory and in particular Eq. (63), the scattering matrix element $S_\ell(k)$ corresponding to Eq. (A1) reads

$$S_\ell(k) = -\frac{h_\ell^{-(d)}(kR)}{h_\ell^{+(d)}(kR)}. \quad (\text{A2})$$

and thus reaches a pole when

$$h_\ell^{+(d)}(kR) = 0. \quad (\text{A3})$$

Using the definition (62), Eq. (A3) can directly be expressed in terms of the Hankel function

$$H_\nu^+(z) = 0, \quad (\text{A4})$$

where $z = kR$ and the order ν is given by Eq. (66). Equation (A4) means that the resonance poles of the hard sphere model are just the zeros of the Hankel function $H_\nu^+(z)$ for $z \in \mathbb{C}$. These zeros have been little considered in the literature. The *NIST Handbook of Mathematical Functions* [24] does not explicitly give quantitative estimates of these zeros, but refers to the more in-depth articles [57, 58]. In particular, the most successful theory describing these zeros seems to be in Ref. [58]. This is thus the main reference of this appendix.

The first zeros of the Hankel function are shown in Fig. 15. Given the relation (66), integer orders corre-

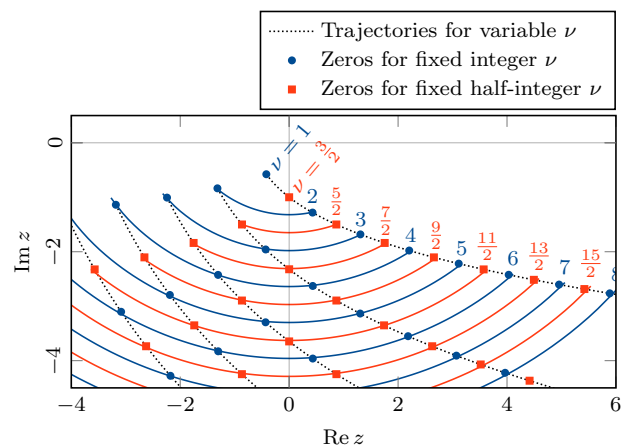


FIG. 15. First complex zeros of the Hankel function $H_\nu^+(z)$ for $\arg z \in [-\pi, 0]$ and for integer and half-integer orders. The dotted curves represent the exact trajectory of the zeros when ν is continuously increased. The colored curves are given by the approximation (A16) for continuous parameter $\tau \in [-\frac{\pi}{2}, \frac{\pi}{2}]$ and fixed values of ν . The other zeros around $\arg z = -\pi$ for $\nu \in \mathbb{Z}$ are not shown.

spond to even dimensions ($d \in \{2, 4, 6, \dots\}$), and half-integer orders to odd dimensions ($d \in \{1, 3, 5, \dots\}$). When ν is relatively large compared to 1, the zeros draw a kind of elliptic arc in the lower half-plane ($\arg z \in [-\pi, 0]$). The size of this arc linearly increases with ν . When ν is half an integer, the zeros are symmetrically placed with respect to the imaginary z axis. It should be

noted that an infinite string of zeros may also exist along the negative real axis ($\arg z = -\pi$) when the order ν is not half an integer. However, we do not consider these additional zeros in this work, because they are too far from the real positive axis ($\arg z = 0$) and not relevant for the numerical simulations. These zeros are thus not shown in Fig. 15. In this section, we restrict ourselves to the arc of zeros for $\arg z \in [-\pi, 0]$.

The idea to solve Eq. (A4) for z is to approximate it by asymptotic expressions valid for large positive ν . The issue is that there is no direct asymptotic expansion for $H_\nu^+(z)$ in the lower half-plane ($\arg z \in [-\pi, 0]$) reliable enough to extract zeros. This is due to the exponentially increasing behavior of $H_\nu^+(z)$ in this region, which hides the zeros. To address this issue, the method proposed in Ref. [58] is to use the analytic continuation formula for $\arg z \in [-\pi, 0]$ [24]

$$H_\nu^+(z) = \frac{2}{\pi} i^{-\nu-1} [\pi I_\nu(e^{i\frac{\pi}{2}} z) + e^{i\pi\nu} K_\nu(e^{i\frac{\pi}{2}} z)] , \quad (\text{A5})$$

where $I_\nu(z)$ and $K_\nu(z)$ are the modified Bessel functions [24]. The branch cut in the right-hand side of Eq. (A5) is located on the semiaxis $\arg z = -\frac{3\pi}{2}$. The advantage of the continuation (A5) is that, in the region of the zeros ($\arg z \in [-\pi, 0]$), the Bessel functions are now evaluated in the right half-plane ($|\arg(iz)| \leq \frac{\pi}{2}$) where useful asymptotic approximations for large ν can be found. In this regard, we will use the approximations

$$\begin{cases} I_\nu(z) \xrightarrow{\nu \gg |z|} \frac{(z/2)^\nu}{\Gamma(\nu+1)} \exp\left(\frac{(z/2)^2}{\nu+1}\right) , \\ K_\nu(z) \xrightarrow{\nu \gg |z|} \frac{\Gamma(\nu)}{2(z/2)^\nu} \exp\left(-\frac{(z/2)^2}{\nu-1}\right) . \end{cases} \quad (\text{A6})$$

As pointed in Ref. [58], it seems that, while being accurate enough to get two decimal places on the sought zeros, expressions (A6) are not mentioned in mathematical handbooks such as Ref. [24]. Using expression (A5), Eq. (A4) becomes

$$\ln\left(\frac{I_\nu(iz)}{K_\nu(iz)}\right) = i\pi(\nu + \frac{1}{2}) - \ln \pi + 2\pi i n \quad \forall n \in \mathbb{Z} , \quad (\text{A7})$$

where we have taken the logarithm, hence the appearance of an arbitrary integer index n . Now, if we substitute the Bessel functions in Eq. (A7) by their approximations (A6), we can write

$$\begin{aligned} 2\nu \ln(iz/2) + \frac{2\nu(iz/2)^2}{\nu^2 - 1} \\ = i\pi(\nu + \frac{1}{2}) + \ln[\Gamma(\nu)\Gamma(\nu+1)] - \ln(2\pi) + 2\pi i n . \end{aligned} \quad (\text{A8})$$

It is worth noting that Eq. (A8) can already be solved exactly for z by means of the Lambert function $W(z)$ defined by [24]

$$W(z) e^{W(z)} = z . \quad (\text{A9})$$

However, further approximations can be done without loss of precision. In particular, the gamma functions can

be approximated by the first three terms of the following Stirling expansion

$$\begin{aligned} \ln[\Gamma(\nu)\Gamma(\nu+1)] &= 2\nu \ln(\nu) - 2\nu + \ln(2\pi) \\ &+ \frac{1}{6\nu} + \mathcal{O}(\frac{1}{\nu^3}) . \end{aligned} \quad (\text{A10})$$

Therefore, Eq. (A8) becomes

$$\ln\left(\frac{iz}{2\nu}\right) + \frac{(iz/2)^2}{\nu^2 - 1} = i\pi \frac{\nu + \frac{1}{2} + 2n}{2\nu} - 1 . \quad (\text{A11})$$

If, in addition, we assume that ν is large enough so that $\nu^2 - 1 \simeq \nu^2$, then it is even more appropriate to define the change of variable

$$x = \frac{iz}{2\nu} . \quad (\text{A12})$$

In contrast to z which increases linearly with ν near the zeros, the new variable x remains more or less constant in absolute value. In addition, x belongs to the right half-plane ($|\arg x| \leq \frac{\pi}{2}$). In order to simplify Eq. (A11), it is convenient to define the angular parameter τ from its right-hand side

$$\tau = \pi \frac{\nu + \frac{1}{2} + 2n}{2\nu} \quad \forall n \in \{-\lfloor \nu + \frac{1}{4} \rfloor, \dots, -1\} . \quad (\text{A13})$$

The integer values of n are chosen such that τ belongs to the interval $[-\frac{\pi}{2}, \frac{\pi}{2}]$. The number of zeros described by this approximation is thus $\lfloor \nu + \frac{1}{4} \rfloor$. However, note that the total number of zeros is not finite when ν is not half an integer. With the two notations x and τ , Eq. (A11) becomes much more readable

$$\ln(x) + x^2 = i\tau - 1 , \quad (\text{A14})$$

where x is the unknown. A first rough estimate of the solution of Eq. (A14) is $x \approx e^{i\tau-1}$. This estimate shows that, when n varies, the zeros draw an elliptic curve close to an arc of circle of radius e^{-1} and angles $\tau \in [-\frac{\pi}{2}, \frac{\pi}{2}]$ in the complex plane of x . In fact, it is possible to solve exactly Eq. (A14) for x with the Lambert $W(z)$ function. We obtain

$$x = \sqrt{\frac{1}{2} W(2e^{2i\tau-2})} \quad \text{for } \arg x \in [-\frac{\pi}{2}, \frac{\pi}{2}] . \quad (\text{A15})$$

Only the principal branch of $W(z)$ must be considered here since the argument is small enough in absolute value compared to the radius of convergence of the Maclaurin series of the Lambert function, which is e^{-1} . This is true because indeed $\tau \in \mathbb{R}$ and $2e^{-2} < e^{-1}$. Finally, using Eq. (A12), we obtain the approximate positions of the zeros of $H_\nu^+(z)$

$$z = -2i\nu \sqrt{\frac{1}{2} W(2e^{2i\tau-2})} , \quad (\text{A16})$$

where τ is given by (A13). Note that other approximations not relying on the Lambert function were proposed

in Ref. [58], but we do not find them useful here because, from a numerical perspective, the Lambert function can be computed very quickly in Maclaurin series

for small arguments, or more generally with the Newton method [24]. Approximation (A16) is all we need for the numerical application considered in Sec. II C for Eq. (65).

-
- [1] L. L. Foldy, Phys. Rev. **67**, 107 (1945).
 - [2] M. Lax, Rev. Mod. Phys. **23**, 287 (1951).
 - [3] M. Lax, Phys. Rev. **85**, 621 (1952).
 - [4] P. C. Waterman and R. Truett, J. Math. Phys. **2**, 512 (1961).
 - [5] V. Twersky, in *Stochastic Processes in Mathematical Physics and Engineering*, Proceedings of Symposia in Applied Mathematics, Vol. 16, edited by R. Bellman (American Mathematical Society, 1964) pp. 84–116.
 - [6] J. M. Ziman, Proc. Phys. Soc. **88**, 387 (1966).
 - [7] E. Akkermans and G. Montambaux, *Mesoscopic Physics of Electrons and Photons*, 1st ed. (Cambridge University Press, 2007).
 - [8] P. Sheng, *Introduction to Wave Scattering, Localization and Mesoscopic Phenomena*, Springer Series in Materials Science, Vol. 88 (Springer, Berlin, 2006).
 - [9] C. W. J. Beenakker, Rev. Mod. Phys. **69**, 731 (1997).
 - [10] M. C. W. van Rossum and T. M. Nieuwenhuizen, Rev. Mod. Phys. **71**, 313 (1999).
 - [11] N. Cherroret, *Coherent transport of waves in random media: from mesoscopic correlations to Anderson localization*, PhD thesis, Université Joseph-Fourier, Grenoble I (2009).
 - [12] S. Chandrasekhar, *Radiative Transfer*, Dover Books on Intermediate and Advanced Mathematics (Dover, 1960).
 - [13] R. L. Fante, J. Opt. Soc. Am. **71**, 460 (1981); J. Opt. Soc. Am. **72**, 815 (1982).
 - [14] V. P. Tishkovets and K. Jockers, J. Quant. Spectrosc. Radiat. Transf. **101**, 54 (2006).
 - [15] A. Doicu and M. I. Mishchenko, J. Quant. Spectrosc. Radiat. Transf. **220**, 123 (2018); J. Quant. Spectrosc. Radiat. Transf. **224**, 25 (2019); J. Quant. Spectrosc. Radiat. Transf. **224**, 154 (2019).
 - [16] M. I. Mishchenko, L. D. Travis, and A. A. Lacis, *Multiple Scattering of Light by Particles: Radiative Transfer and Coherent Backscattering* (Cambridge University Press, 2006).
 - [17] D. Gaspard and J.-M. Sparenberg, Phys. Rev. A **105**, 042204 (2022), arXiv:2111.03136 [quant-ph].
 - [18] D. Gaspard and J.-M. Sparenberg, Phys. Rev. A **105**, 042205 (2022), arXiv:2111.04410 [quant-ph].
 - [19] D. Gaspard, MSMModel - Program for solving multiple-scattering problems, GitHub repository (2023), version v1.0.0.
 - [20] E. Anderson, Z. Bai, C. Bischof, S. Blackford, J. Demmel, J. Dongarra, J. Du Croz, A. Greenbaum, S. Hammarling, A. McKenney, and D. Sorensen, *LAPACK Users' Guide*, 3rd ed. (Society for Industrial and Applied Mathematics, Philadelphia, 1999).
 - [21] D. V. Kupriyanov, I. M. Sokolov, and M. D. Havey, Phys. Rep. **671**, 1 (2017).
 - [22] D. Gaspard, Phys. Rev. A **106**, 062211 (2022), arXiv:2209.02056 [quant-ph].
 - [23] D. Gaspard and J.-M. Sparenberg, Phys. Rev. A **107**, 022214 (2023), arXiv:2211.14816 [quant-ph].
 - [24] F. W. J. Olver, D. W. Lozier, R. F. Boisvert, and C. W. Clark, *NIST Handbook of Mathematical Functions*, 1st ed. (Cambridge University Press, 2010).
 - [25] H. C. van de Hulst, *Light Scattering by Small Particles*, Dover Books on Physics (Dover Publications, 1981) originally published by Wiley, 1957.
 - [26] D. Gaspard, *Quantum Scattering, Transport, and Decoherence in Disordered Media: An Application to Gaseous Particle Detectors*, PhD thesis, Université libre de Bruxelles (2022).
 - [27] P. W. Anderson, Phys. Rev. **109**, 1492 (1958).
 - [28] B. Kramer and A. MacKinnon, Rep. Prog. Phys. **56**, 1469 (1993).
 - [29] A. Lagendijk, B. van Tiggelen, and D. S. Wiersma, Phys. Today **62**, 24 (2009).
 - [30] C. Miniatura, R. C. Kuhn, D. Delande, and C. A. Müller, Eur. Phys. J. B **68**, 353 (2009).
 - [31] I. Plante and F. A. Cucinotta, New J. Phys. **11**, 063047 (2009).
 - [32] R. E. Kennerly, Phys. Rev. A **21**, 1876 (1980).
 - [33] E. Rutherford, Sci. Mon. **18**, 337 (1924).
 - [34] M. Snee and W. Ubachs, J. Quant. Spectrosc. Radiat. Transf. **92**, 293 (2005).
 - [35] N. Dunford, J. T. Schwartz, W. G. Bade, and R. G. Bartle, *Linear Operators, Part 1: General Theory*, Pure and Applied Mathematics, Vol. 7 (Interscience Publishers, New York, 1958).
 - [36] L. Tsang and A. Ishimaru, J. Opt. Soc. Am. A **1**, 836 (1984).
 - [37] P.-E. Wolf and G. Maret, Phys. Rev. Lett. **55**, 2696 (1985).
 - [38] E. Akkermans, P. E. Wolf, and R. Maynard, Phys. Rev. Lett. **56**, 1471 (1986).
 - [39] B. A. van Tiggelen, A. Lagendijk, and A. Tip, J. Phys.: Condens. Matter **2**, 7653 (1990).
 - [40] A. Lagendijk and B. A. van Tiggelen, Phys. Rep. **270**, 143 (1996).
 - [41] E. E. Salpeter and H. A. Bethe, Phys. Rev. **84**, 1232 (1951).
 - [42] A. M. Weinberg and E. P. Wigner, *The Physical Theory of Neutron Chain Reactors*, University of Chicago Committee on Publications in the Physical Sciences (University of Chicago Press, 1958).
 - [43] S. M. Barnett, S. Franke-Arnold, A. S. Arnold, and C. Baxter, J. Phys. B: At. Mol. Opt. Phys. **33**, 4177 (2000).
 - [44] M. Born and E. Wolf, *Principles of Optics: 60th Anniversary Edition*, 7th ed. (Cambridge University Press, 2019).
 - [45] K. Hornberger, in *Entanglement and Decoherence: Foundations and Modern Trends*, Lecture Notes in Physics, Vol. 768, edited by A. Buchleitner, C. Viviescas, and M. Tiersch (Springer, Berlin, 2009) Chap. 5.
 - [46] I. Kamleitner, *Open Quantum System Dynamics from a Measurement Perspective: Applications to Coherent Particle Transport and to Quantum Brownian Motion*, PhD thesis, Macquarie University (2010), arXiv:1009.4349

- [quant-ph].
- [47] T. Juffmann, H. Ulbricht, and M. Arndt, Rep. Prog. Phys. **76**, 086402 (2013).
 - [48] E. J. Heller, Phys. Rev. Lett. **53**, 1515 (1984); Phys. Scr. **T90**, 154 (2001).
 - [49] H. van Beijeren and J. R. Dorfman, J. Stat. Phys. **108**, 767 (2002).
 - [50] K. B. Efetov, *Supersymmetry in Disorder and Chaos* (Cambridge University Press, Cambridge, 1997).
 - [51] Y. V. Nazarov and Y. M. Blanter, *Quantum Transport: Introduction to Nanoscience* (Cambridge University Press, Cambridge, 2009).
 - [52] Y. V. Fyodorov, M. A. Skvortsov, and K. S. Tikhonov, arXiv:2211.03376 [cond-mat.dis-nn] (2022).
 - [53] C. J. Joachain, *Quantum Collision Theory*, 2nd ed. (North-Holland, Amsterdam, 1979).
 - [54] R. G. Newton, *Scattering Theory of Waves and Particles*, 2nd ed., Dover Books on Physics (Dover, Mineola, 1982).
 - [55] J. R. Taylor, *Scattering Theory: The Quantum Theory of Nonrelativistic Collisions*, Dover Books on Engineering (Dover Publications, Mineola, 2006).
 - [56] J. J. Sakurai and J. Napolitano, *Modern Quantum Mechanics*, 3rd ed. (Cambridge University Press, 2020).
 - [57] A. Cruz and J. Sesma, Math. Comput. **39**, 639 (1982).
 - [58] M. K. Kerimov and S. L. Skorokhodov, USSR Comput. Math. Math. Phys. **24**, 115 (1984).